Monthly Notices
of the
ROYAL ASTRONOMICAL SOCIETY

Mon. Not. R. Astron. Soc. **427,** 1953–1972 (2012) doi:10.1111/j.1365-2966.2012.22006.x

The low-mass end of the fundamental relation for gravitationally lensed star-forming galaxies at $1 < z < 6$⋆

Lise Christensen,[1,2]† Johan Richard,[1,3] Jens Hjorth,[1] Bo Milvang-Jensen,[1] Peter Laursen,[1,4] Marceau Limousin,[5] Miroslava Dessauges-Zavadsky,[6] Claudio Grillo[1,2] and Harald Ebeling[7]

[1]*Dark Cosmology Centre, Niels Bohr Institute, University of Copenhagen, Juliane Maries Vej 30, 2100 Copenhagen, Denmark*
[2]*Excellence Cluster Universe, Technische Universität München, Bolzmanstrasse 2, 85748 Garching, Germany*
[3]*Centre de Recherche Astrophysique de Lyon, Université Lyon 1, Observatoire de Lyon, 9 Avenue Charles André, 69561 Saint Genis Laval cedex, France*
[4]*Oskar Klein Centre, Department of Astronomy, Stockholm University, SE-10691 AlbaNova, Stockholm, Sweden*
[5]*Aix Marseille Université, CNRS, LAM (Laboratoire d'Astrophysique de Marseille) UMR 7326, 13388 Marseille, France*
[6]*Observatoire de Genève, Université de Genève, 51 Ch. des Maillettes, 1290 Sauverny, Switzerland*
[7]*Institute for Astronomy, University of Hawaii, 2680 Woodlawn Drive, Honolulu, HI 96822, USA*

Accepted 2012 August 29. Received 2012 August 28; in original form 2012 June 26

ABSTRACT

We present Very Large Telescope/X-shooter spectra of 13 galaxies in the redshift range $1 \lesssim z \lesssim 6$, which are strongly lensed by massive galaxy clusters. Spectroscopic redshifts are measured for nine galaxies, while three sources have redshifts determined from continuum breaks in their spectra. The stellar masses of the galaxies span four orders of magnitude between 10^7 and 10^{11} $M_\odot$ and have luminosities at 1500 Å rest frame between 0.004 and $9L^*$ after correcting for the magnification. This allows us to probe a variety of galaxy types from young, low-mass starburst galaxies to massive evolved galaxies. The lensed galaxies with stellar masses less than 10^{10} $M_\odot$ have a large scatter compared to the fundamental relation between stellar mass, star formation rates and oxygen abundances. We provide a modified fit to the fundamental relation for low-mass, low-metallicity galaxies with a weaker dependence of the metallicity on either the star formation rate or stellar mass compared to low-redshift, high-mass and high-metallicity Sloan Digital Sky Survey galaxies.

Key words: gravitational lensing: strong – galaxies: abundances – galaxies: distances and redshifts – galaxies: evolution – galaxies: high-redshift.

1 INTRODUCTION

Strong gravitational lensing is an important tool for characterizing the dark matter distribution and formation of large mass concentrations in a Λ cold dark matter (ΛCDM) framework. Since massive galaxy clusters give rise to magnification factors of 10–50 of background galaxies, as well as stretching the source images into extended arcs, lensing can be used to characterize the physical properties of intrinsically subluminous galaxies and investigate spatially resolved properties of high-redshift galaxies (Swinbank et al. 2007). Gravitational lensing is also valuable for locating $z > 6$ galaxies (Bradley et al. 2008; Richard et al. 2011b; Zitrin et al. 2012a) and investigate individual galaxies which may be representative of those responsible for reionization.

The Lyman break technique by construction selects galaxies with similar characteristics, such that their stacked spectra can be analysed (Shapley et al. 2003). Individual galaxies are too faint for spectroscopic studies with reasonable use of telescope time, apart from unusually bright Lyman break galaxies (LBGs; Erb et al. 2010). Other selection techniques have been used to study the fainter end of the high-redshift galaxy luminosity function, including Lyman α (Lyα) emitters (e.g. Fynbo et al. 2003; Nilsson et al. 2011) or host galaxies of gamma-ray bursts (GRBs; e.g. Hjorth et al. 2012). However, they fail to reach the same level of detail because of the large amount of telescope time needed. Our current understanding of the physical properties of high-redshift galaxies is therefore limited to a small range in absolute magnitude.

Gravitational lensing allows us to study intrinsically fainter galaxies with unusual spectral characteristics at any given redshift, although most lensed galaxies studied in detail to date still belong to

⋆Based on data from the X-shooter GTO observations collected at the European Southern Observatory VLT/Kuyuen telescope, Paranal, Chile, under programme IDs: 084.B-0351(D), 086.A-0674(A), 086.A-0674(B), 087.A-0432(A) and 087.A-0432(B). Based on *HST* general observer programmes GO-10491, GO-11103 and GO-12166.

†E-mail: lise@dark-cosmology.dk

the high-mass, high-luminosity end. A few cases have provided a great deal of insight into the physical properties of individual $z = 2$–3 galaxies, with the prime example being the lensed galaxy MS 1512-cB58 (Pettini et al. 2000, 2002; Teplitz et al. 2000). The past few years have seen a steady increase in the number of spectroscopic observations of lensed galaxies at $z \sim 2$ either detected serendipitously or in large dedicated surveys (Fosbury et al. 2003; Cabanac et al. 2005; Allam et al. 2007; Swinbank et al. 2007; Stark et al. 2008; Diehl et al. 2009; Lin et al. 2009; Bian et al. 2010; Richard et al. 2011a; Rigby et al. 2011; Wuyts et al. 2012b). Whereas some $z = 2$ lensed galaxies are easily investigated with low-resolution spectra from 8-m class telescopes, few are sufficiently bright for medium- or high-resolution spectroscopy, which is necessary for examining the interstellar medium (ISM) of the galaxy. Rest-frame ultraviolet (UV) absorption line spectra allow a detailed analysis of the ISM of galaxies with intrinsically very high star formation rates (SFRs; Cabanac, Valls-Gabaud & Lidman 2008; Quider et al. 2009, 2010; Dessauges-Zavadsky et al. 2010).

As the redshift around $z \sim 2$ represent the era of the peak of the star formation, the lensed galaxies are relevant to compare to scaling relations found in other galaxy samples, such as mass–metallicity relations (Tremonti et al. 2004). Recently, a fundamental relation between the mass, metallicity and SFR has been found. The relation has been calibrated for metal rich [oxygen abundances $12+\log(\mathrm{O/H}) > 8.2$], and relatively massive galaxies (stellar masses above $10^{9.2}\,\mathrm{M}_{\odot}$) at $z < 0.1$ (Lara-López et al. 2010). At higher redshifts up to $z \approx 2.5$ and for galaxies with lower metallicities the relation appears to still hold (Mannucci et al. 2010). Strong gravitational lensing of intrinsically fainter and less massive galaxies allows us to explore the fundamental relation at even lower masses and metallicities. Richard et al. (2011a) and Wuyts et al. (2012b) analysed the rest-frame optical emission lines of lensed galaxies at $z = 1$–3 with intrinsic low luminosities ($0.1L^*$) and showed that the galaxies are more metal rich than predicted from extrapolations of mass–metallicity relations.

In this paper, we present shallow spectroscopic observations from Very Large Telescope (VLT)/X-shooter of 13 lensed galaxies selected towards massive galaxy clusters at $z \sim 0.4$. Section 2 presents the data and Section 3 notes on each target and their redshift determination. In Section 4 we explore the galaxy properties from their continuum, while in Section 5 we derive physical properties based on their emission lines. In Section 6 we present an extension of the calibration at the low-mass, low-metallicity end of the fundamental relation for star-forming galaxies. Section 7 presents a summary.

2 OBSERVATIONAL DATA

One of the science goals for the second generation VLT instrument X-shooter is to determine redshifts for faint single targets and analyse emission-line galaxies at $z > 1$. X-shooter is a multiwavelength cross-dispersed echelle spectrograph which splits up the light by dichroics into three arms: UV-blue (UVB), which covers 3000–5600 Å, visible-R (VIS), which covers 5600–10 000 Å, and near-IR (NIR), which covers from 1 to 2.5 μm (D'Odorico et al. 2006; Vernet et al. 2011). The slit length of X-shooter is 11 arcsec and the chosen slit widths determine the spectral resolution. For the observations the slit widths were set to match the optical seeing measured at the telescope as listed in Table 1. Slit widths of 1.0/0.9/0.9 arcsec in the UVB, VIS and NIR arms, give spectral resolutions of 5100, 8800 and 5600, respectively, while for the 1.3/1.2/1.2 arcsec slit widths, the resolutions are 4000, 6700 and 4300. For all the observations, the UVB CCD was read out binned by a factor of 2 in the dispersion direction.

The instrument has proven to be useful for the study of gravitational lensed galaxies due to its complete wavelength coverage and high sensitivity throughout the spectral range. Physical properties of lensed galaxies can be derived from short exposures as demonstrated from commissioning data (Christensen et al. 2010; Dessauges-Zavadsky et al. 2010; Pettini et al. 2010). A wealth of information of the physical properties of galaxies can be gained from the full medium-resolution UV to NIR spectral coverage for both lensed galaxies such as the 8 o'clock arc (Dessauges-Zavadsky et al. 2010, 2011) or even fainter GRB host galaxies (Krühler et al. 2012). With the large wavelength coverage, X-shooter is also ideal to determine faint galaxy redshifts, which is necessary to construct the lens models (e.g. Grillo & Christensen 2011). Because of the simultaneous coverage, there are no random offsets in the placement of the slit between the three arms, which could be a problem for optical spectra and NIR spectra obtained with different instruments. Such offsets could introduce differences in the flux levels between the UV and NIR galaxy spectra which are difficult to correct for unless the continuum emission is well detected and can be compared with broad-band photometry. In addition, systematic errors in wavelength calibrations could be interpreted as kinematic effects such as outflows. X-shooter is therefore ideal for the combined purpose of determining redshift for faint, lensed sources, and allows a characterization of the physical nature of the lens galaxies.

Accurate mass models of the lensing clusters are required in order to turn them into well-calibrated gravitational telescopes because

Table 1. Observing log.

Cluster	Arc ID	RA (J2000)	Dec. (J2000)	Slit angle (°)	Slit widths (arcsec)	UVB/VIS/NIR exposures (s)	Date (dd–mm–yyyy)
Abell 1689	4.1	13:11:32.17	−01:20:57.3	−19.4	1.3/1.2/1.2	2 × 3000/2 × 3000/6 × 520	22–03–2010
Abell 1689	8.1	13:11:32.30	−01:20:50.8				
Abell 1689	9.1	13:11:30.30	−01:19:48.33	18.8	1.3/1.2/1.2	2 × 3000/2 × 3000/6 × 520	22–03–2010
Abell 1689	31.1	13:11:30.42	−01:19:51.5				
SMACS J0304.3−4402	1.1	03:04:20.29	−44:02:27.8	90	1.0/0.9/0.9	4 × 900/4 × 900/4 × 900	30–08–2011
MACS J0329.6−0211	1.2	03:29:40.18	−02:11:45.8	112	1.0/0.9/0.9	4 × 1200/4 × 1200/4 × 1200	30–08–2011
SMACS J0359.2−7205	1.1	03:59:13.46	−72:05:14.6	49	1.0/0.9/0.9	3 × 900/3 × 900/3 × 900	30–08–2011
MACS J0416.1−2403	1.1	04:16:09.85	−24:03:42.5	−160	1.0/0.9/0.9	8 × 800/8 × 770/8 × 900	13–01–2011
MACS J1115.8+0129	1.1	11:15:51.40	01:29:36.6	–30	1.0/0.9/0.9	4 × 800/4 × 770/4 × 900	12–01–2011
MACS J1206.2–0847	2.1/3.1	12:06:14.47	−08:48:33.3	40	1.3/1.2/1.2	4 × 1070/4 × 1100/4 × 1200	03–04–2011
MACS J1311.0−0310	1.1	13:11:01.37	−03:10:50.3	90	1.0/0.9/0.9	4 × 800/4 × 770/4 × 900	03–04–2011
SMACS J2031.8−4036	1.1	20:31:52.89	−40:37:32.6	0	1.0/0.9/0.9	4 × 800/4 × 770/4 × 900	11–10–2010
MACS J2129.4−0741	1.5	21:29:26.07	−07:41:41.6	0	1.0/0.9/0.9	4 × 800/4 × 770/4 × 900	11–10–2010

of the degeneracy between the source redshift and lens mass. To determine redshifts of lensed galaxies do not require high signal-to-noise ratio (S/N) spectra, and since the UV-selected high-redshift galaxies are expected to be star forming, and therefore have emission lines that are much stronger than the underlying continuum, a redshift determination can be obtained even for faint ($m = 25$) galaxies with a short integration time. With fairly short exposures, we can pinpoint interesting targets for deeper follow-up studies.

2.1 Target selection

Some of the best calibrated cluster lenses are the $z < 0.3$ Abell clusters. In this paper, we present spectra of galaxies without previously determined spectroscopic redshifts lensed by Abell 1689, where we aim to determine spectroscopic redshift for galaxies which previously only had photometric redshifts. Partly, we focus on the second large-scale dark matter concentration in the north-east quadrant of the cluster (Limousin et al. 2007), such that the galaxy scale mass substructure can be better constrained in this region.

We also choose to study galaxies lensed by higher redshift clusters. We select targets belonging to the Massive Cluster Survey (MACS), which are massive X-ray luminous clusters at $0.3 < z < 0.7$ (Ebeling, Edge & Henry 2001), and include observations of the southern equivalent to the MACS with declinations $<-40^{\circ}$ (Ebeling, unpublished). These targets are denoted with the prefix SMACS. Some of the targets are also included in the Cluster Lensing And Supernova survey with Hubble (CLASH; Postman et al. 2012), allowing us to investigate in detail galaxies for which high-quality, high-resolution images are available. Although the 16 broad-band filter imaging allows detailed investigations of the spectral energy distribution (SED) of the galaxies and their spatially resolved properties, more accurate information can be obtained by spectroscopic follow-up observations. The target galaxies are selected from having high total brightness, and from those we investigate regions with the highest surface brightness. This implies that we preferentially select UV bright galaxies that are expected to show significant emission lines, because the high surface brightness regions are H II regions. Thereby, we can most easily determine redshifts for the faintest galaxies, and also investigate the kinematics and metal abundances in the emission-line regions.

2.2 Spectroscopic observations and data reduction

The observations were done as a part of the X-shooter consortium guaranteed observing time during several different runs in 2010–2011. A log of the observations can be found in Table 1. The names of the arcs targeted for the spectroscopic analysis are hereafter shortened, such that the names reflect the cluster name only for the MACS clusters, i.e. the arc observed in SMACS J0304.3−4402 is named M0304, and the arcs in Abell 1689 are denoted 'A' plus by their IDs, e.g. A4.1. In Table 1 and hereafter we adopt the image IDs from Limousin et al. (2007) for Abell 1689 images, IDs for M0329 in Zitrin et al. (2012a), IDs for M1206 from Zitrin et al. (2012b) and the ID for M2129 in Zitrin et al. (2011).

For target acquisition, relative offsets from bright stars were used, so the location of the target on the slit depends on the accuracy of the known star coordinates relative to the targets. The slit position angle was not preferentially chosen along the long axis of the extended arcs. In most cases, we chose a perpendicular angle such that nodding the target along the slit would improve the residuals from sky emission-line subtraction. Further, the angle was chosen to avoid nearby objects. The orientations of the slits are overlayed on the panels in Fig. 1. A different procedure was used during the first run, when the Abell 1689 cluster arcs were observed, where we opted for longer time on target in stare-mode and did not move the target along the slit. In addition, two arcs from different sources were inside the slit. Whereas this procedure did allow us to determine the arc redshifts, the quality of the NIR spectra after the data reduction was dominated by errors in sky subtraction, in particular near sky emission lines. No separate sky exposures were obtained.

The data were reduced with the ESO pipeline version 1.3.7 (Goldoni et al. 2006; Modigliani et al. 2010) using the physical model reduction chain (Bristow et al. 2008) in both nodding and staring mode. The data reduction works in a similar way for the three arms. First, the bias level is subtracted from the UVB and VIS data (dark current in the case of the NIR data). The position of the orders on the detectors was traced and a two-dimensional (2D) flat-field was created. Then a 2D wavelength solution was determined from calibration frames taken the day after the observations. Cosmic rays were rejected from the science frames using the LA COSMIC procedure (van Dokkum 2001) within the pipeline. Finally, the echelle orders were extracted, rectified and merged on to a 2D spectrum using the errors as weights for the region of the overlap between the different orders.

2.3 Further data processing

The data from the pipeline needed a few more processing steps before a full analysis could be done. To determine spatial offsets along the slit between each exposure, one could rely on FITS header information, or measure offsets directly from the data. We chose the latter, but because the continuum emission was very faint, this was only possible after binning the 2D data as described in Section 2.3.1. Individually reduced 2D spectra were combined using their errors as weights.

One-dimensional (1D) spectra were extracted by co-adding rows of data. For each object, the apertures were chosen visually from the binned 2D spectra with an aperture size matching for the three arms. Typically, an aperture size of 1–2 arcsec was used. Source 8.1 in Abell 1689, where the X-shooter slit was oriented along the arc, was noticeably more extended in the 2D spectrum, and an aperture of 4 arcsec was used.

Flux calibration was performed with standard procedures in IRAF. Observations of various spectrophotometric standard stars (GD 71, LTT 3218 and EG 274) with a 5 arcsec wide slit taken at the night of the observations were used to calibrate the transmission in each of the arms. Reference fluxes for these stars covering the UV to the NIR were taken from Bohlin, Dickinson & Calzetti (2001) and Vernet et al. (2008). A correction for an average atmospheric extinction measured at Paranal (Patat et al. 2011) was applied to the data. M1206, M1311, M2031 and M2129 were observed in non-photometric conditions. Since the fluxes in the X-shooter spectrum were corrected to absolute values by the magnitudes measured in *Hubble Space Telescope* (*HST*) images, flux calibration errors would be partly mitigated as the line fluxes were corrected for slit losses. Even though the slit orientation was not equal to the parallactic angle, differential slit losses should be minor effect, since X-shooter has an atmospheric dispersion corrector in the UVB and VIS arms. The NIR arm does not have a corrector for atmospheric dispersion, but since the observations were done at airmasses below 1.6 the effect was also minor. The X-shooter pipeline gives as an output the wavelength solution measured in air, which we correct to vacuum heliocentric frame before deriving redshifts. Finally, the

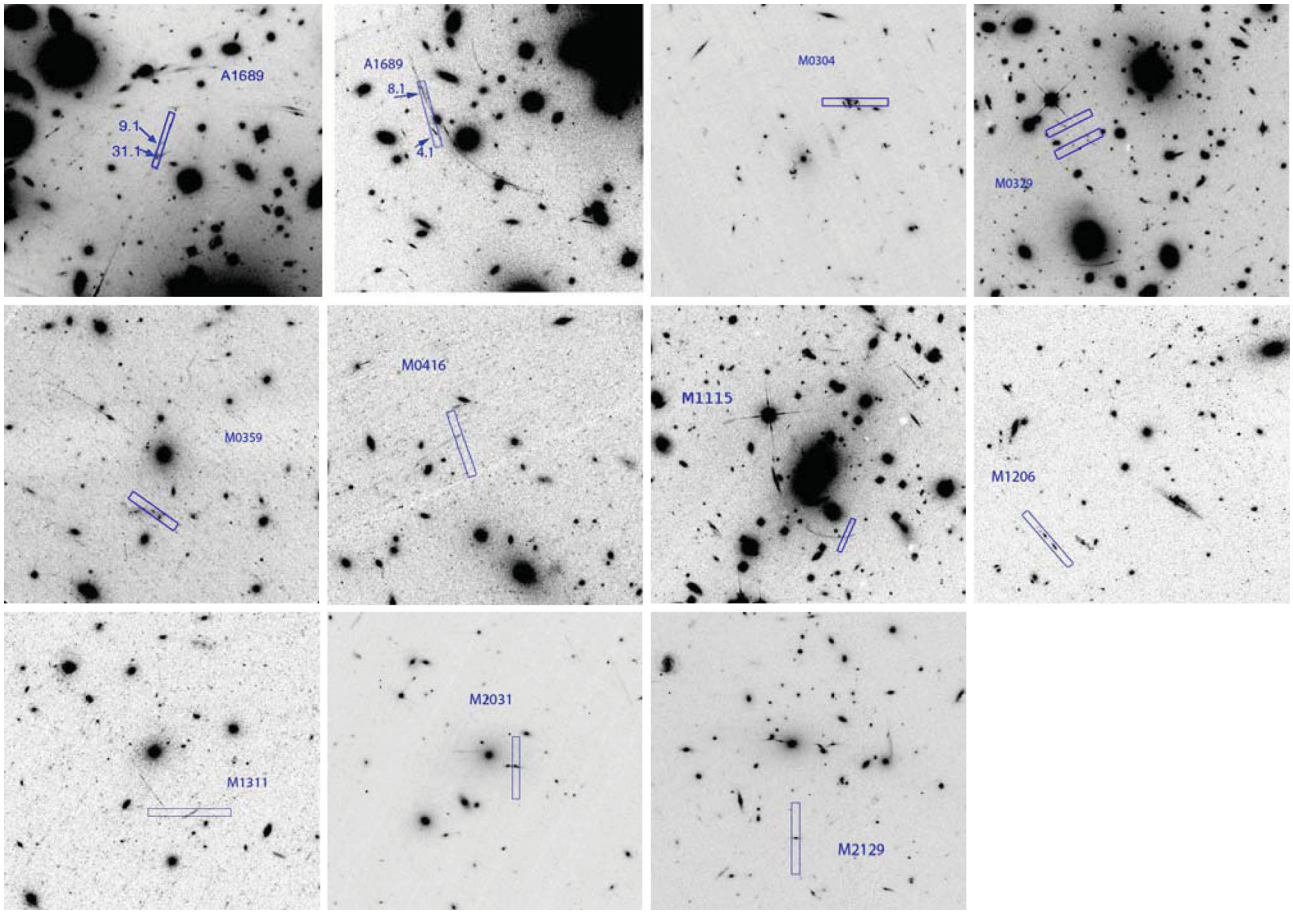

Figure 1. Thumbnail *HST* images of the clusters around the targeted sources. The images were taken with ACS, WFPC2 or WFC3 with either the *F606W*, *F814W* or *F110W* filters, and obtained through the Mikulski Archive for Space Telescopes (MAST) or Hubble Legacy Archive (HLA) data archive (http://hla.stsci.edu/). The images have varying sizes between 40 and 90 arcsec on a side with the orientation north up and east left, and with the X-shooter 11 arcsec slit position indicated.

spectra were corrected for Galactic reddening using the dust maps of Schlegel, Finkbeiner & Davis (1998).

The extracted and flux-calibrated spectra show small offsets in the continuum flux between the different arms. In particular, the VIS to the NIR differs by 10–20 per cent in some cases, but given the low S/Ns of the spectra, the flux levels were not adjusted. The continuum emission follows the expectations over the entire wavelength range as illustrated in Fig. 2. In addition to these small offsets, the flux calibration showed increased errors at the edges of the spectral ranges in each arm, where the total transmission is very small due to the dichroic crossover between the arms. The spectra in these affected regions are excluded in Fig. 2.

Emission lines were identified by visual inspection, and line fluxes were measured with NGAUSSFIT within IRAF, assuming that the line profiles have a Gaussian shape. In some cases of very strong lines, the lines are clearly not Gaussian, but can be fit well with a combination of two Gaussian functions (see also Christensen et al. 2010; Pettini et al. 2010). In those cases the listed fluxes correspond to the sum of the two components. Uncertainties of the line width, height and continuum level are propagated for the derivation of emission-line flux uncertainties. Some of the faintest lines have a more uncertain determination of the peak emission wavelength, which implies an apparent shift in redshift compared to the brightest lines. The shifts can be up to $\sim$100 km s^{-1}, but is unphysical if we assume that the lines arise in the same medium. We determine source redshifts from the mean weighted by the line flux, which overcomes the problem of the small variation of redshift. Balmer emission lines are affected by underlying stellar absorption. In order to correct for this, we subtracted a stellar population model described in Section 4.1 from the galaxy spectrum to get a pure emission-line spectrum before fitting the emission lines.

Removal of telluric absorption lines for the low S/N data increases significantly the noise in the data. Instead of correcting the full 1D spectra, which would introduce additional errors in the spectra, we chose to correct only the emission-line fluxes individually when necessary. To correct for this absorption, we used data of bright, hot stars, observed immediately before or after the science exposure and at the same airmass. The instrument set-up was the same, and the data were reduced in the same way as the science frames. A 1D spectrum of the star was extracted, normalized, and the 1D science spectrum divided by this normalized spectrum. Regions where the atmospheric transmission was less than 5 per cent was set to zero, and when fitting emission lines, these regions were excluded.

2.3.1 *Optimal 2D spectral binning*

Observations in the NIR from the ground are heavily affected by the strong sky emission lines which vary with time. However, bluewards of 2.2 μm, the continuum emission from the sky between the sky lines presents a minor contribution. This is the purpose of the design

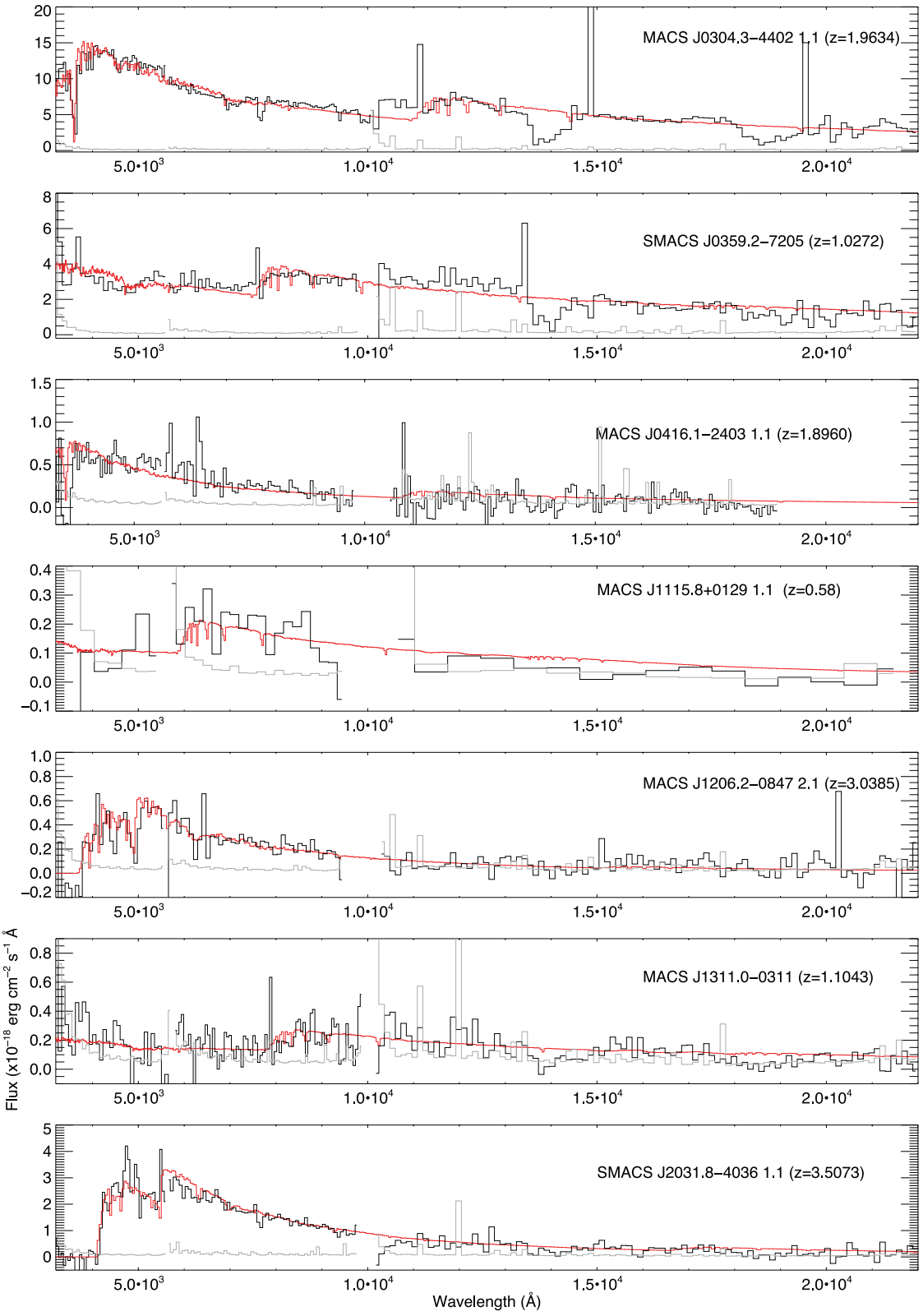

Figure 2. Binned source spectra with the best-fitting spectral templates overplotted by the red lines (Section 4.1). The grey lines are the error spectra. Regions with very noisy data are omitted, both in the fitting and in the display. In particular, wavelengths at 1 μm between the VIS and the NIR arm are dominated by uncertainties in the flux calibration. See the electronic issue of the paper for a colour version of this figure. The continuum emission in the NIR for the Abell 1689 arcs is considerably more noisy compared to the other spectra due to increased sky subtraction errors.

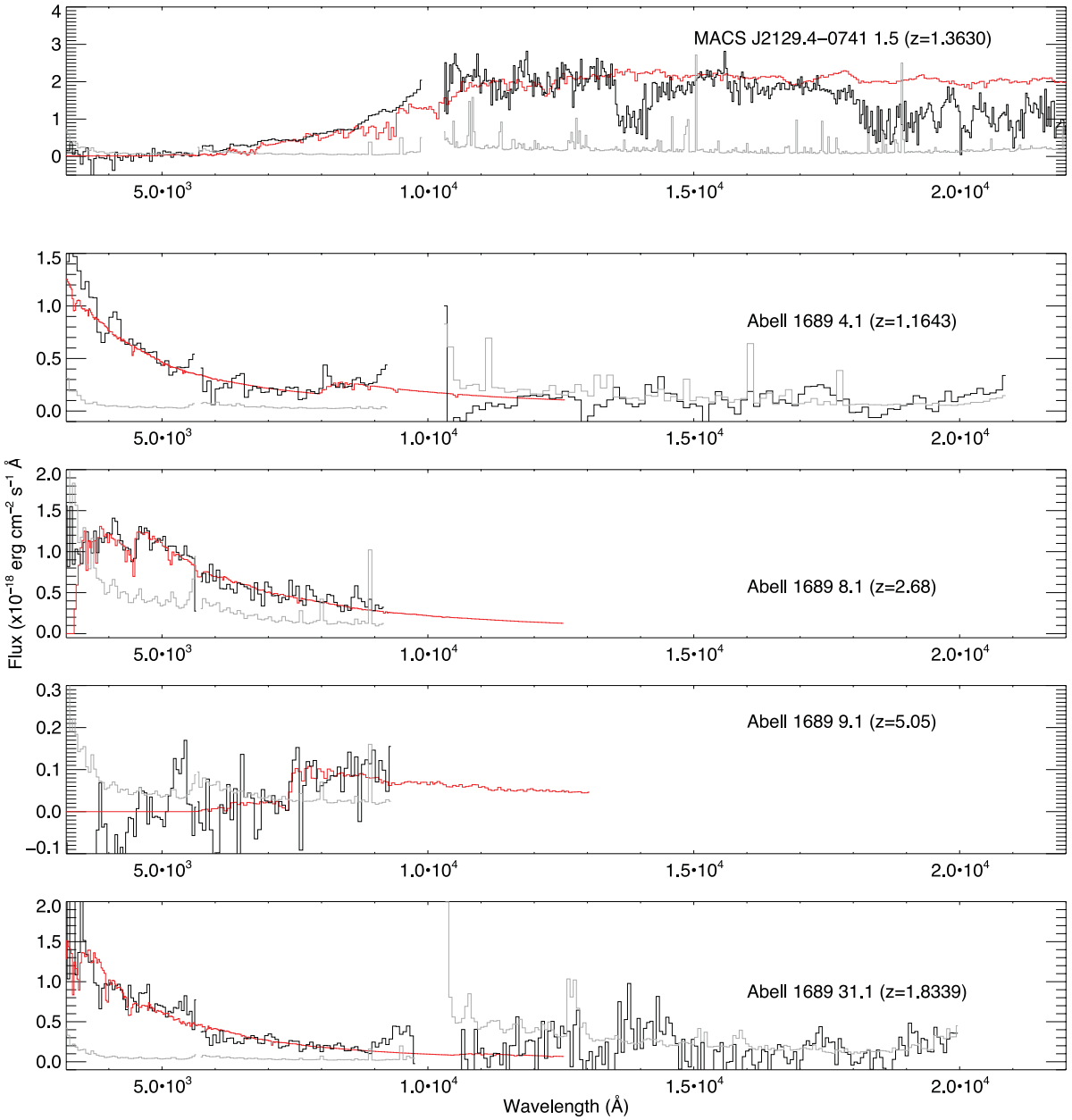

Figure 2 – *continued*

of X-shooter; at a sufficiently high spectral resolution, one can eliminate the regions of sky lines, and co-add the remaining part of the spectrum to obtain a much deeper detection limit than would otherwise have been possible as long as the detector read noise does not dominate over the background sky emission.

With this basic principle, we can use the X-shooter data to detect very faint objects. In practise, we take the 2D spectra and the associated 2D error spectra and bin the data by any required amount using a weighted mean algorithm. This binning effectively smoothes out any spectral characteristics, so depending on the type of investigation, we choose a binning factor between 1 (for investigating absorption lines and very weak emission lines) and ∼200 Å pixel^{-1} (for investigating the continuum emission from the faintest targets). The latter flux calibrated 1D spectra for the arcs are presented in Fig. 2.

2.4 High-resolution images

Since the targets are lensed by well-studied massive galaxy clusters, most of these have extensive high spatial resolution images already available in the *HST* archive. Both deep and snapshot images with the Wide Field Planetary Camera 2 (WFPC2), Advanced Camera for Surveys (ACS) or Wide Field Camera 3 (WFC3) instruments have been taken. We obtained these images from the *HST* archive, and used SExtractor (Bertin & Arnouts 1996) to derive the photometry of the sources as listed in Table 2. Up to date zero-points were used, and the fluxes were corrected to total magnitude measured in the detection band (*I* band). For the most extended arcs SExtractor was first used to subtract the extended emission from brighter galaxies in the field to create a residual image free of emission from the lens galaxies. Then we defined a polygon around the extended arc in the deepest image and derived the magnitude in the other filters

Table 2. Total AB magnitudes of the arcs.

Cluster	Arc ID	*F475W*	*F606W*	*F625W*	*F775W*	*F814W*	*F850LP*	Camera
A1689	4.1	24.29 ± 0.11	–	24.06 ± 0.10	23.78 ± 0.08	–	23.42 ± 0.13	ACS
A1689	8.1	23.29 ± 0.06	–	22.69 ± 0.04	22.45 ± 0.04	–	22.40 ± 0.08	ACS
A1689	9.1	>28.2	–	>27.9	25.75 ± 0.09	–	25.89 ± 0.15	ACS
A1689	31.1	24.02 ± 0.07	–	24.27 ± 0.12	24.08 ± 0.11	–	24.74 ± 0.29	ACS
M0304	1.1	–	20.19 ± 0.06					ACS
M0359	1.1		21.58 ± 0.05	–	–	–	–	WFPC2
M0416	1.1	–	23.27 ± 0.09	–	–	23.73 ± 0.12	–	WFPC2
M1115	1.1	23.00 ± 0.41	23.80 ± 0.10	22.94 ± 0.37	23.69 ± 0.40	23.40 ± 0.6	–	ACS
M1206	2.1	24.91 ± 0.05	23.16 ± 0.05	24.24 ± 0.05	23.12 ± 0.02	22.99 ± 0.01	23.19 ± 0.03	ACS
M1311	1.1		22.58 ± 0.13					WFPC2
M2031	1.1	–	21.19 ± 0.10	–	–	–	–	ACS
M2129	1.5	–	–	–	23.48 ± 0.14	23.04 ± 0.09	22.69 ± 0.15	ACS
Cluster	Arc ID	*F105W*	*F110W*	*F125W*	*F140W*	*F160W*		Camera
M0329	1.1/1.2		25.0 ± 0.3					WFC3
M1115	1.1	–	22.94 ± 0.33	22.86 ± 0.20	22.54 ± 0.18	22.20 ± 0.22		WFC3
M1206	2.1	23.13 ± 0.02	23.13 ± 0.02	23.21 ± 0.02	23.12 ± 0.02	23.10 ± 0.02		WFC3
M2129	1.5	21.50 ± 0.05	21.05 ± 0.05	20.72 ± 0.05	20.33 ± 0.05	19.97 ± 0.01		WFC3

using the same polygon as reference. The photometric uncertainties were determined from photon noise measured in the original images before drizzling. In the case of Abell 1689 ID 9.1, the photometry was defined for a point source as the 3σ limiting magnitude in the measured aperture.

2.4.1 Slit losses

Besides the loss of flux in slit spectra since some emission fall outside the slit due to the seeing effects and inaccuracy of the centring on the slit, the lensed images also experience slit losses due to their extended and arc-like nature. Some of the observed images appear as compact sources even though they are stretched by the lensing effects, while other images are much extended low surface brightness arcs. Therefore we determine in each case the fraction of light falling within the slit relative to the total flux in each band. The flux-calibrated spectrum is multiplied with the respective filter transmission function to derive the magnitude and the slit losses are calculated for each filter. The final, wavelength-independent correction factor to be applied to the spectra is the weighted average of the factors in all measured bands, $f_{\rm slit}$, as listed in Table 3, where the weight in each band determined from the sum of the square of the photometric uncertainties in Table 2 and the uncertainty derived from the associated 1D error spectrum.

Table 3. Lens image slit loss and image magnification factors, μ.

Lens image	ID	$f_{\rm slit}$	μ
Abell 1689	4.1	2.7 ± 0.1	23.0 ± 3.4
Abell 1689	8.1	2.9 ± 0.7	38.9 ± 4.0
Abell 1689	9.1	1.0 ± 0.1	12.7 ± 2.8
Abell 1689	31.1	1.7 ± 0.1	26.6 ± 3.1
SMACS 0304	1.1	3.0 ± 0.1	42.0 ± 8.0
SMACS 0359	1.1	3.0 ± 0.1	18.0 ± 6.0
MACS 0416	1.1	2.6 ± 0.3	4.6 ± 0.2
MACS 1115	1.1	5.0 ± 1.7	16.3 ± 1.4
MACS 1206	2.1	5.1 ± 0.2	9.2 ± 0.6
MACS 1311	1.1	12.7 ± 5.3	28.0 ± 12.0
SMACS 2031	1.1	4.2 ± 0.3	15.8 ± 7.0
MACS 2129	1.5	2.1 ± 0.1	9.4 ± 2.0

Properties derived from spectra obtained in non-photometric conditions are partly recovered from the correction of slit losses, since the method we adopt does not discriminate between losses of light falling outside the slit or loss of light due to absorption by clouds. However, since we only apply a constant offset to the flux calibration, a wavelength-dependent error caused by the non-photometric conditions could be introduced. Also, galaxies have colour gradients, but we do not include corrections based on these gradients in this investigation.

2.5 Lens models

High spatial resolution images are crucial information for the analysis of gravitational lensing. The relative projected positions of the lens and source galaxies along with spectroscopic (or photometric) redshifts are necessary ingredients to determine the total mass distribution of the lenses. The lens models allow us to reconstruct the original images of the galaxies in the source plane before lensing, to derive their radius, which is essential to derive dynamical masses.

In this paper, we use mass models constructed using the LENSTOOL software (Jullo et al. 2007)[1] based on the multiple images observed in the *HST* images. The detailed LENSTOOL model of A1689 has been published by Limousin et al. (2007) and the models for the MACS clusters will be presented elsewhere (Richard et al., in preparation). We summarize here the main ingredients of the models. Our starting point is the set of multiple systems identified in the *HST* images (between one and seven systems) which complete the ones presented by other groups (Ebeling et al. 2009; Zitrin et al. 2011, 2012a,b). The majority of these systems have been confirmed with a measured spectroscopic redshift, including the ones obtained from X-shooter and presented in this paper. We use the positions and redshifts of these systems to constrain a multicomponent mass distribution described as a parametric model, including both cluster-scale and galaxy-scale components (see Richard et al. 2010, for more details). The Monte Carlo Markov chain sampler created by LENSTOOL provides us with a family of best models fitting the constraints, allowing us to derive for each parameter its 1σ error bar. The estimate on the magnification factors and their corresponding errors are

[1] Publicly available at http://lamwws.oamp.fr/lenstool/

Table 4. Cluster and arc redshifts.

Cluster	$z_{\rm cluster}$	Arc ID	$z_{\rm em}$	$z^a_{\rm break}$	$z_{\rm abs}$
A1689	0.181	4.1	1.1643 ± 0.0001^b		
A1689		8.1		2.68 ± 0.04	
A1689		9.1		5.05 ± 0.02	
A1689		31.1	1.8339 ± 0.0003^c		1.8348 ± 0.0012
SMACS J0304.3−4402	0.3–0.5	1.1	1.9634 ± 0.0002		1.9635 ± 0.0005
MACS J0329.6−0211	0.45	1.1/1.2	–		
SMACS J0359.2−7205	0.296	1.1	1.0272 ± 0.0005		
MACS J0416.1−2403	0.420	1.1	1.8960 ± 0.0003		
MACS J1115.8+0129	0.355	1.1		0.58 ± 0.02 or 3.51 ± 0.01	
MACS J1206.2−0847	0.439	2.1/3.1	3.0385 ± 0.0001^d		3.0372 ± 0.0015
MACS J1311.0−0310	0.494	1.1	1.1043 ± 0.00002		
SMACS J2031.8−4036	0.331	1.1	3.5073 ± 0.0002		3.5061 ± 0.0013
MACS J2129.4−0741	0.589	1.5	1.3630 ± 0.0004		1.3617 ± 0.0012

Notes. Cluster redshifts are from Abell, Corwin & Olowin (1989) and for M1115 and M1206 in Ebeling et al. (2010), and M2129 in Ebeling et al. (2007). M0359 and M2031 cluster redshifts are based on ESO/EMMI and FORS archive spectra. The redshift of the M0304 cluster is measured from photometry.
Other source spectroscopic redshifts: [a]redshifts based on spectral modelling; [b]Jullo et al. (2010) report $z = 1.1648$; [c]Broadhurst et al. (2005) report $z = 1.83$; [d]Zitrin et al. (2012b) report $z = 3.033$.

provided for each target in Table 3. In the case of SMACS 0304, the uncertainty in the cluster redshift (estimated between 0.3 and 0.5) is taken into account when deriving the magnification factor of the target 1.1 in this cluster. With the information of the total flux from the galaxies including the effect of magnification and slit losses, we can derive the absolute properties of the galaxies.

3 SOURCE SPECTRA

In this section we present notes for each of the observed arcs. Table 4 summarizes the measured redshifts for the arcs from emission and absorption lines, as well as redshifts derived from breaks in highly binned spectra, when no clear emission or absorption lines could be distinguished. Individual tables in this section list the detected emission lines and their fluxes uncorrected for magnification or slit losses. Typically, only few absorption lines are found by visual inspection for some of the galaxies, because the S/N level in the continuum is low, and the absorption redshift corresponds to the average of the detected lines. As a consequence of the low S/N levels, the uncertainties of the absorption line redshifts are higher than those based on emission lines.

3.1 Abell 1689 arc ID 4.1

Two different lensed images (source IDs 4.1 and 8.1) were placed within the X-shooter slit. The names of the sources are adopted from Limousin et al. (2007). Source ID 4.1 is reported to have $z = 1.1648$ (Jullo et al. 2010), and is located at the lower edge of the slit during the observations, and sky subtraction errors are high in the NIR arm. From the flux-weighted average of the emission lines in Table 5, we measure the redshift $z = 1.1643 \pm 0.0001$.

Among the other strong optical emission lines that fall within the spectral range, Hβ is behind a strong sky line, the [N II] $\lambda\lambda$6548, 6583 and [S II] $\lambda\lambda$6717, 6730 doublets are affected by telluric absorption lines so their fluxes are below the detection limit.

In the 2D spectrum we detect the emission from a third object located 2 arcsec north of A4.1. An extended early-type galaxy is located at RA = 13:11:32.14, Dec. = −01:20:55.33 (J2000) in the ACS image, but it is only partly covered by the slit. After rebinning the 2D spectrum a clear break is seen at 4400 Å, consistent with a Balmer jump at the Abell 1689 redshift. In the spectrum of the third object we detect the Ca II $\lambda\lambda$3934, 3639 absorption doublet at $z = 0.170$ and a single emission line at 7682 Å consistent with Hα at $z = 0.1702$.

Table 5. Emission lines from the A1689 arc ID 4.1.

Line	$\lambda^a_{\rm r}$	$\lambda_{\rm obs}$	z	Flux[b]
[O II]	3727.09	8066.41	1.16427	11.8 ± 0.2
[O II]	3729.88	8072.44	1.16426	15.6 ± 0.2
[Ne III]	3869.84	8375.75	1.16436	3.7 ± 0.5
Hδ	4102.92	8880.27	1.16438	1.8 ± 0.6
Hγ	4341.69	9396.41[c]	1.16423	5.7 ± 1.1
[O III]	4960.29	10 735.74[d]	1.16434	15.4 ± 1.9
[O III]	5008.24	10 840.01[d]	1.16444	39.8 ± 2.4
Hα	6564.63	14 208.28[c]	1.16437	51.5 ± 4.4

[a]Rest-frame vacuum wavelengths.
[b]Emission-line flux in units of 10^{-18} erg cm^{-2} s^{-1}.
[c]Affected by strong telluric absorption lines.
[d]Close to sky line.

3.2 Abell 1689 arc ID 8.1 (giant arc)

Despite being a giant arc, the redshift of image ID 8.1 remains to be measured accurately. Broadhurst et al. (2005) give the best-fitting photometric redshift $z_{\rm phot} = 2.63 \pm 0.48$ while Halkola, Seitz & Pannella (2006) find $z_{\rm phot} = 3.10 \pm 0.89$ and Limousin et al. (2007) determine $z = 2.30 \pm 0.21$ based on their lens model.

The object is located at the upper edge of the slit, and is affected by sky subtraction residuals, which limit our ability to get redshift information from absorption lines. A faint continuum is detected in the binned 2D spectrum. With a binning factor of 200 and 400 pixels in the UVB and VIS arms, respectively, any weak and narrow emission or absorption lines are effectively smoothed out. No emission lines are detected above a 3σ level significance in the unbinned spectrum.

The binned UVB and VIS spectrum of ID 8.1 is extracted within a 4-arcsec aperture and displayed in Fig. 2. The flux-calibrated spectrum shows no clear Lyman limit break; however, we find indications of a break at 4470 Å. If we in interpret this break as the onset of the Lyα forest, it implies a redshift of $z = 2.68 \pm 0.04$ by fitting

stellar population synthesis spectra as described in Section 4.1. The lack of a detected Lyman limit break is due to the high noise level at wavelengths shorter than 3500 Å.

3.3 Abell 1689 arc ID 9.1

Source ID 9.1 is recognized as an *F625W* drop-out in the ACS images, and has a photometric redshift of 5.16 ± 0.74 and an AB magnitude of 25.9 in the *F775W* band (Broadhurst et al. 2005). Halkola et al. (2006) find a similar photometric redshift 4.97 ± 0.78, while lens models predict a lower redshift $z_{\rm model} = 2.69 \pm 0.27$ (Limousin et al. 2007).

Two sources (IDs 9.1 and 31.1) were located within the X-shooter slit as illustrated in Fig. 1. The spatial offset between source IDs 9.1 and 31.1 projected on the sky is 2.5 arcsec as measured in an ACS image. The A9.1 continuum spectrum is faint, and corresponds to an AB magnitude of 26.6 ± 0.4 at ∼8000 Å, but is detected in the binned frames illustrated in Fig. 2, where we identify a break at 7381 Å. If the break corresponds to the onset of the Lyα forest it implies $z = 5.05 \pm 0.02$. Neither Lyα emission line nor any other significant spectral features are present at these faint flux levels.

3.4 Abell 1689 arc ID 31.1

The arc ID 31.1 is adopted from Limousin et al. (2007), who argued that the three images of source ID 12 in Broadhurst et al. (2005) are inconsistent with being the same galaxy. The source 31.1 was located close to the edge of the slit, where sky subtraction errors were higher than the average.

A wealth of emission lines are detected as listed in Table 6. Excluding Lyα while weighting the other emission-line redshift by their measured fluxes, we find $z = 1.8339 \pm 0.0003$, consistent with that reported in Broadhurst et al. (2005) and Limousin et al. (2007). The Lyα line profile is double peaked with a brighter red than blue component and has an equivalent width of 40 Å. We detect several uncommon emission lines for this source. In particular we draw attention to the O III] λλ1661, 1666 and C IV λλ1548, 1550 doublets, which indicate the presence of a strong ionizing source. These lines were also detected in another lensed galaxy (Fosbury et al. 2003; Villar-Martín, Cerviño & González Delgado 2004). The temperature-sensitive [O III] λ4363 line is rarely detected in galaxies at $z > 1$. Yuan & Kewley (2009) find this line in another lensed galaxy at $z = 1.7$, also behind the Abell 1689 cluster. In a separate paper we present a more detailed analysis of the emission from this unusual galaxy (Christensen et al. 2012).

Table 6. Emission lines from the A1689 arc ID 31.1.

Line	$\lambda_{\rm r}^a$	$\lambda_{\rm obs}$	z	Flux^b
Lyα	1215.67	3445.77	1.8345	72.7 ± 0.7
C IV	1548.20	4386.81	1.833 49	4.3 ± 0.4
C IV	1550.77	4394.22	1.833 57	4.7 ± 0.3
O III]	1660.81	4705.82	1.833 45	3.2 ± 0.4
O III]	1666.15	4720.63	1.833 26	7.4 ± 0.3
[C III]	1906.68	5402.29	1.833 35	9.1 ± 0.4
C III]	1908.73	5408.19	1.833 40	4.7 ± 0.4
[O II]	3727.09	10 563.06	1.834 13	9.2 ± 0.8
[O II]	3729.88	10 569.40	1.833 71	11.7 ± 0.9
[Ne III]	3869.84	10 965.28	1.833 52	6.4 ± 2.5
Hγ	4341.69	12 301.90	1.833 44	17.0 ± 2.1
[O III]	4364.44	12 366.36	1.833 44	6.2 ± 1.8
Hβ	4862.70	13 777.99^c	1.833 40	42.7 ± 4.9
[O III]	4960.29	14 057.55^c	1.834 02	63.0 ± 10.6
[O III]	5008.24	14 194.09^{c,d}	1.834 15	211.5 ± 5.7

[a]Rest-frame vacuum wavelengths.
[b]Emission-line flux in units of 10^{-18} erg cm^{-2} s^{-1}.
[c]Affected by strong telluric absorption lines.
[d]Close to sky line.

Table 7. Emission lines from the M0304 arc ID 1.1.

Line	$\lambda_{\rm r}^a$	$\lambda_{\rm obs}$	z	Flux^b
O III]	1660.81	4921.93	1.96357	7.1 ± 1.6
O III]	1666.15	4937.35	1.96333	11.4 ± 1.9
[O II]	2470.22	7322.39	1.96337	8.4 ± 2.1
[O II]	3727.09	11 044.78	1.96331	437.8 ± 3.4
[O II]	3729.88	11 053.09	1.96332	587.2 ± 3.9
H9	3836.49	11 370.55^c	1.96372	29.1 ± 4.2
[Ne III]	3869.84	11 468.93^c	1.96360	149.9 ± 3.8
He I + H8	3890.17	11 527.64^c	1.96320	95.3 ± 3.2
[Ne III]	3968.53	11 761.36	1.96359	64.3 ± 3.4
H7	3971.20	11 767.48	1.96313	51.8 ± 1.7
Hδ	4102.92	12 158.43	1.96329	128.5 ± 2.7
Hγ	4341.69	12 866.19	1.96333	205.9 ± 1.3
Hβ	4862.70	14 410.72^c	1.96345	500.0 ± 0.9
[O III]	4960.29	14 700.41^c	1.96355	669.5 ± 1.9
[O III]	5008.24	14 841.33^c	1.96331	2357 ± 3.5
He I	5877.28	17 417.44	1.96345	47.0 ± 5.2
Hα	6564.63	19 453.85^c	1.96336	1802.1 ± 0.6
[N II]	6585.42	19 513.96^c	1.96313	58.1 ± 2.7
[S II]	6718.29	19 910.44	1.96355	156.8 ± 1.1
[S II]	6732.67	19 951.76	1.96335	102.7 ± 1.7

[a]Rest-frame vacuum wavelengths.
[b]Emission-line flux in units of 10^{-18} erg cm^{-2} s^{-1}.
[c]Affected by telluric absorption lines.

3.5 SMACS J0304.3−4402 arc ID 1.1

The morphology of the lensed galaxy is complex, and likely consists of several components that are in the process of a merger. In each of the lensed image counterparts in the *HST* image, five individual regions are visible. The X-shooter spectrum of the source includes three of these regions. Because of blending by the seeing, however, only two regions are spatially distinguishable in the 2D spectrum. Many strong rest-frame optical emission lines are detected from this galaxy at $z = 1.9634 \pm 0.0002$ as listed in Table 7 including again the O III] λλ1661, 1666 doublet. The emission lines from the two regions have a velocity offsets of ∼100 km s^{-1}, while the UV continuum appears similar in shape. The emission-line fluxes in Table 7 are the total flux in the X-shooter slit summed for the two regions. Even though the Balmer lines are very bright from this source, Lyα emission is absent, and its (UV) spectrum appears similar to the cB58 spectrum (Pettini et al. 2000). A more detailed investigation is presented in Christensen et al. (2012).

3.6 MACS J0329.6−0211 arc ID 1.1/1.2

The two mirrored lensed images with IDs 1.1. and 1.2, which have a photometric redshift of $z = 6.18^{+0.07}_{-0.05}$ (Zitrin et al. 2012a), were targeted by the observations, which were carried out by both nodding and offsetting along the slit. The galaxy has a high surface brightness region at the edges pointing towards each other, and a more elongated lower surface brightness region in the extended arcs. The slit orientation covered only the high surface brightness regions, where the brightest image ID 1.2 has a magnitude of 25.0 AB mag

Table 8. Emission lines from the M0359 arc ID 1.1.

Line	λ_r^a	λ_{obs}	z	Flux^b
[O II]	3727.09	7558.09	1.02788	97.7 ± 3.2
[O II]	3729.88	7560.08	1.02690	137.9 ± 3.4
[Ne III]	3968.53	8048.88	1.02818	5.0 ± 1.7
Hδ	4101.74	8317.41	1.02778	11.0 ± 2.5
Hγ	4341.69	8800.95	1.02708	37.1 ± 1.6
Hβ	4862.70	9856.80	1.02702	95.4 ± 1.4
[O III]	5008.24	10 152.15	1.02709	87.9 ± 4.0
[N II]	6549.91	13 276.12^c	1.02692	23.8 ± 3.8
Hα	6564.63	13 306.85^c	1.02705	369.1 ± 0.9
[N II]	6585.42	13 348.02^c	1.02690	55.4 ± 4.4
[S III]	9533.20	19 324.30^c	1.02705	56.4 ± 4.0

^{a}Rest-frame vacuum wavelengths.
^{b}Emission-line flux in units of 10^{-18} erg cm^{-2} s^{-1}.
^{c}Affected by telluric absorption lines.

in the *F110W* image (see Zitrin et al. 2012a, for photometric data of all lensed images).

We detect neither emission lines nor the continuum emission even in a highly binned 2D spectrum. With the faintness of the galaxy, we do not expect to detect the continuum emission even with a very large binning factor, but aim instead for a detection of a single emission line. We would be able to detect Lyα in the VIS arm to a 3σ significance level of 5×10^{-18} erg cm^{-2} s^{-1} assuming a typical line width of 50 km s^{-1}. We cannot exclude that an emission line happens to fall directly at the wavelength of a strong sky emission line given the uncertainty of the photometric redshift. In that case, the 3σ detection limit could be much higher: $\sim 2 \times 10^{-16}$ erg cm^{-2} s^{-1}.

3.7 SMACS J0359.2−7205 arc ID 1.1

Emission lines from this arc are listed in Table 8. No unusual strong UV emission lines are detected even though its low redshift ($z = 1.0272 \pm 0.0005$) and the wavelength coverage would allow for detection of the [C III], C III] doublet. [O III] λ4959 lies in a very noisy region where the transmission of the NIR arm is low and is not detected.

3.8 MACS J0416.1−2403 arc ID 1.1

Emission lines detected from this arc at $z = 1.48960 \pm 0.0003$ are listed in Table 9. Hβ and the [O III] λλ4959, 5007 doublet are strongly affected by telluric absorption lines, and the correction for the atmospheric absorption implies a correction factor between 3 and 10. The flux uncertainty only reflects the emission-line fitting, since the error for the correction for telluric lines is not propagated. Again, no strong UV emission lines are detected, because even the strongest rest-frame optical lines are relatively faint.

Table 9. Emission lines from the M0416 arc ID 1.1.

Line	λ_r^a	λ_{obs}	z	Flux^b
[O II]	3727.09	10 793.11	1.89585	17.2 ± 1.4
[O II]	3729.88	10 801.18	1.89585	24.5 ± 1.4
Hβ	4862.70	14 081.70^c	1.89586	27.4 ± 2.1
[O III]	4960.29	14 367.79^c	1.89656	27.2 ± 2.8
[O III]	5008.24	14 503.75^c	1.89598	100.2 ± 4.2

^{a}Rest-frame vacuum wavelengths.
^{b}Emission-line flux in units of 10^{-18} erg cm^{-2} s^{-1}.
^{c}Affected by strong telluric absorption lines.

3.9 MACS J1115.8+0129 arc ID 1.1

The image of the source is a very low surface brightness arc. The X-shooter slit was oriented across the arc so the slit losses were substantial.

We do not detect any emission lines in either of the arms. The continuum emission is the faintest among our sample, and is only recognizable after binning the spectrum by a factor >20 along the dispersion. The binned extracted spectrum in Fig. 2 is extracted with an aperture of 1.5 arcsec. The NIR spectrum is also very faint, but the continuum emission is detected in the binned spectrum although it is too faint to be detected in the *K* band. Between the UVB and VIS spectra, there appears to be a break, which we can interpret either as the Balmer decrement at $z \approx 0.5$, or a higher redshift for the onset of the Lyα forest at $z \approx 3.5$. The exact wavelength of the break is sensitive to the binning of the data; a smaller binning suggests a higher break wavelength, and thus a higher redshift. Leaving the redshift as a free parameter in HyperZ (Bolzonella, Miralles & Pelló 2000), we determine the galaxy redshift $z = 0.58 \pm 0.02$ or $z = 3.51 \pm 0.01$. The physical properties of the galaxy derived in Section 4 depend on the assumed redshift, and we suggest that the lowest redshift is valid one based on the lensing model.

3.10 MACS J1206.2−0847 arc IDs 2.1 and 3.1

The conditions during the observations were poor with changing seeing and thin cirrus clouds. The slit orientation was chosen such that the two components, denoted by source IDs 2.1 and 3.1 in Zitrin et al. (2012b), which are separated by 2.3 arcsec, were placed within the slit. The two sources have the same redshift (Zitrin et al. 2012b).

We only detect a single, but remarkably bright emission line at 20 220 Å, as illustrated in Fig. 3, and a break in the continuum around 3700 Å. The line is identified as [O III] λ5007 at $z = 3.038$. At this redshift, all the other strong rest-frame optical emission lines ([O II] λλ3727, 3730, Hβ and [O III] λ4959) fall at the wavelengths of sky emission lines or are affected by telluric absorption. At weaker significance, we detect absorption lines at $z = 3.0372 \pm 0.0015$ in the binned spectra illustrated in Fig. 4. The marked lines

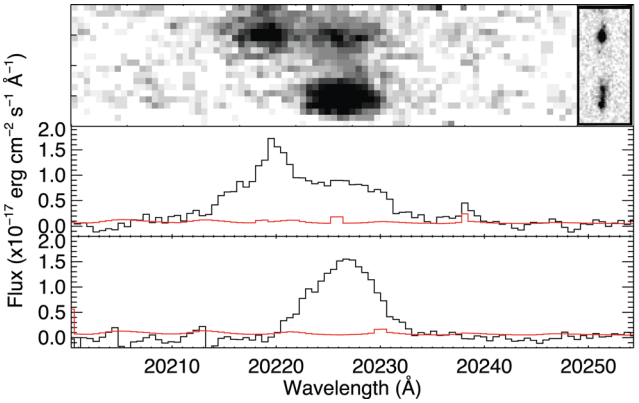

Figure 3. Upper panels: 2D X-shooter spectrum around the single emission line detected for the M1206 source, and the corresponding region around the source in an *HST*/ACS/*F606W* image. The two source IDs 2.1 and 3.1 are separated by 2.3 arcsec and are seen in both panels. Source 2.1 to the north-east in Fig. 1 (upper part in this image) has a compact morphology, and source 3.1 to the south-western one is more extended. The 1D spectra in the middle and lower panels are extracted for each of the sources and are corrected for telluric absorption lines.

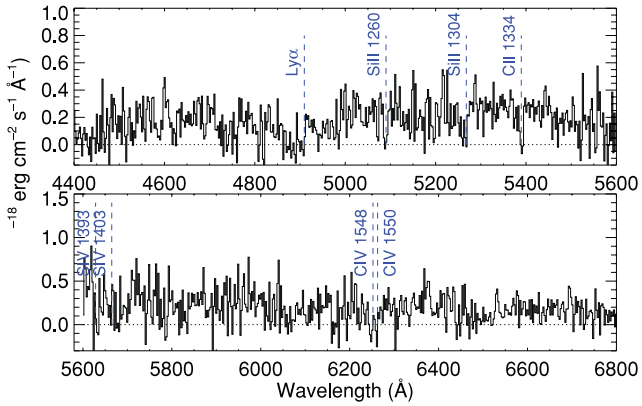

Figure 4. Section of the UVB and VIS spectra of the M1206 source ID 2.1 binned by 10 and 20, respectively, to a dispersion of 2.5 Å pixel^{-1}. Typical strong UV absorption lines seen in high-redshift galaxies are marked at the redshift $z = 3.0385$.

Table 10. Emission lines from the M1206 arc. Source IDs are adopted from Zitrin et al. (2012b).

Line	λ_r^a	λ_{obs}	z	Flux^b
Source ID 2.1				
[O III]	5008.24	20 217.87	3.03696	83.4 ± 1.4
[O III]	5008.24	20 225.77	3.03854	101.9 ± 1.8
Source ID 3.1				
[O III]	5008.24	20 226.02	3.03859	119.7 ± 1.2

^{a}Rest-frame vacuum wavelengths.
^{b}Emission-line flux in units of 10^{-18} erg cm^{-2} s^{-1}.

are the strongest UV lines detected in other high-redshift galaxies, such as in the cB58 galaxy (Pettini et al. 2002). It appears that Lyα is seen in emission at the red wing of a damped Lyα absorption trough, however, the emission line is less significant, and cannot be discerned in the unbinned 1D or 2D spectra. The inferred redshift is consistent with that measured with low-resolution optical spectra only (Zitrin et al. 2012b).

The emission-line profile of the compact north-east image ID 2.1 appears to be double peaked, while the source ID 3.1 only shows one as illustrated in Fig. 3. The separation of the two emission components in the 2.1 source is 7.9 ± 0.3 Å corresponding to a velocity separation of 117 ± 5 km s^{-1}.

The emission-line fluxes in Table 10 include the uncertainties from fitting Gaussian profiles to the observations, but they do not include the uncertainty due to the non-photometric conditions during the observations. The line fluxes are derived after correction for telluric lines, which absorb between 40 and 60 per cent of the emission.

3.11 MACS J1311.0−0310 arc ID 1.1

From the emission lines listed in Table 11 we derive a weighted redshift average of $z = 1.10433 \pm 0.00002$. At this redshift Hα and [N II] fall in the region between the *J* and *H* bands where telluric absorption is severe. The observing conditions were non-photometric, which affect the absolute values of the emission lines. We note that the ratios of emission lines is most likely not affected, because the transmission derived from the spectrophotometric standard star observed during the night appeared similar in shape to that of other nights.

Table 11. Emission lines from the M1311 arc.

Line	λ_r^a	λ_{obs}	z	Flux^b
[O II]	3727.09	7843.14	1.10436	8.0 ± 1.3
[O II]	3729.88	7848.85	1.10432	12.0 ± 0.4
Hβ	4862.70	10 232.73	1.10433	30.6 ± 2.6
[O III]	5008.24	10 539.05	1.10434	13.9 ± 2.4

^{a}Rest-frame vacuum wavelengths.
^{b}Emission-line flux in units of 10^{-18} erg cm^{-2} s^{-1}.

Table 12. Emission lines from the M2031 arc.

Line	λ_r^a	λ_{obs}	z	Flux^b
Lyα	1215.67	5480.80	3.50845	173.7 ± 0.5
N IV]	1486.50	6700.85	3.50780	7.6 ± 0.9
O III]	1660.81	7485.15	3.50693	2.9 ± 0.6
O III]	1666.15	7509.46	3.50707	8.8 ± 0.7
[C III]	1906.68	8594.04	3.50733	12.0 ± 0.5
C III]	1908.73	8603.54	3.50747	8.4 ± 0.9
[O II]	3727.09	16 800.18	3.30759	14.4 ± 1.6
[O II]	3729.88	16 811.01	3.50712	15.5 ± 1.3
[Ne III]	3869.84	17 442.96	3.50741	14.8 ± 2.1
H I (H7)	3971.20	17 898.76	3.50714	6.0 ± 1.0
Hβ	4862.70	21 917.47	3.50726	37.7 ± 1.3
[O III]	4960.29	22 357.68	3.50733	61.9 ± 0.9
[O III]	5008.24	22 573.68	3.50731	205.2 ± 0.5

^{a}Rest-frame vacuum wavelengths.
^{b}Emission-line flux in units of 10^{-18} erg cm^{-2} s^{-1}.

3.12 SMACS J2031.8−4036 arc ID 1.1

Several emission lines are detected from this arc as listed in Table 12, and the flux-weighted average redshift is $z = 3.5073 \pm 0.0002$. Most lines are not affected by telluric absorption, but H I λ3971 has a significant correction, and the flux in Table 12 gives the flux after the correction is applied. Apart from that, telluric absorption and sky emission lines affect our ability to detect Hγ and Hδ, which fall in the region between the *H* and *K* bands.

Again in this case, the Lyα emission-line profile is double peaked, and a wealth of information can be derived from the UV emission lines, which is presented in a separate paper (Christensen et al. 2012). The redshift listed in Table 12 for Lyα reflects the redshift of the bluest wavelength of the red peak as identified by visual inspection.

At the low S/N per pixel in the UVB and VIS arms, we can only identify several Lyman forest absorption lines, and Si II λ1206 and S IV λλ1394, 1403 at $z = 3.5$. A detailed analysis of the absorption lines requires a spectrum with a higher S/N measured in the continuum.

3.13 MACS J2129−0741 arc ID 1.5

The galaxy cluster MACS J2129.4−0741 at $z = 0.589$ shows a galaxy lensed in six distinct images. Zitrin et al. (2011) predict a source redshift of $z = 1.0$–1.5 based on their lens model. The galaxy is red, has colours similar to the lens galaxies and its morphology is consistent with being an early-type galaxy.

For the X-shooter observations, we targeted the isolated, southern-most image of the six. Although it is not the brightest

Table 13. Emission lines from the M2129 arc.

Line	λ_r^a	λ_{obs}	z	Flux^b
[O II]	3727.09	8805.93	1.36251	8.6 ± 1.2
[O II]	3729.88	8814.78	1.36315	7.5 ± 1.1
[O III]	5008.24	11 834.63	1.36314	36.5 ± 1.7

[a]Rest-frame vacuum wavelengths.
[b]Emission-line flux in units of 10^{-18} erg cm^{-2} s^{-1}.

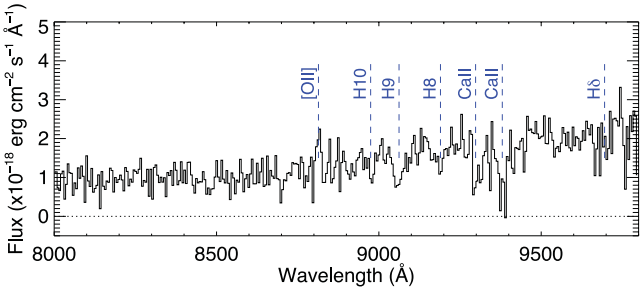

Figure 5. Section of the VIS spectrum of the M2129 arc ID binned to a dispersion of 5.2 Å pixel^{-1}, respectively. Detections of Ca II λλ3934, 3969 lines and absorption lines from the Balmer series of hydrogen at $z = 1.3617$ are indicated. Also a faint emission line from the [O II] λ3727 doublet is visible in this binned version.

of the images, source blending and background subtraction is not a problem at this location. In the extracted spectra we find weak oxygen emission lines listed in Table 13. These lines imply a redshift $z = 1.3630 \pm 0.0004$. At this redshift, absorption lines from Ca II λλ3934, 3969 are detected after telluric absorption lines between 9300 and 9500 Å are corrected for, and several Balmer series absorption lines are also detected (see Fig. 5).

4 PHYSICAL PROPERTIES FROM THE CONTINUUM EMISSION

In this section we derive physical properties based on the continuum spectra from the sources.

4.1 Stellar population fit

To determine the stellar masses of the galaxies, along with other parameters, we use SED fitting methods. Conventionally, SED fits make use of sparsely sampled photometric data from broad- or narrow-band imaging data, whereas we here are dealing with the entire spectral range from the observed UV to NIR. Since the spectra have low S/N, we first bin the data by a factor of between 100 and 1000, depending on the initial quality of the spectra, giving resolutions in the range ∼20–200. The binned spectra and the associated error spectra are shown in Fig. 2.

We compare the spectra with a large set of model spectra from Bruzual & Charlot (2003). We extract spectral templates with 0.2, 0.4 and 1.0 solar metallicities, and star formation histories described as an instantaneous burst or exponentially declining SFRs with e-folding time-scales of 10, 50, 100, 300, 500 and 1000 Myr, and exponentially increasing SFRs with time-scales of 10, 50 and 500 Myr. The initial mass function (IMF) is either a Salpeter (Salpeter 1955) or a Chabrier IMF (Chabrier 2003) with lower and upper mass cut-offs of 0.1 and 100 $M_\odot$, respectively. The best fits are determined by minimizing

$$\chi^2 = \sum_\lambda ((f_{obs,\lambda} - f_{model,\lambda})/\sigma_{obs,\lambda})^2,$$

where the sum is taken over all photometric points, λ in the spectra. In practise, there is no significant distinction between the quality of the fits between the two IMFs. We therefore choose to only use the Chabrier IMF to derive the stellar masses for consistency. If a Salpeter IMF is selected instead, the stellar mass is a factor 1.7 higher due to the flattening of the Chabrier IMF below 1 $M_\odot$.

To determine the best-fitting spectral template, the flux at each (binned) wavelength is converted to an AB magnitude, and we use a modified version of HyperZ (Bolzonella et al. 2000), which allows us to include for each object a catalogue which contains up to 500 individual photometric data points. From all the photometric points between 3000 and 22000 Å, we exclude the wavelengths around 1 μm, where the flux calibration causes inaccuracies at the wavelengths where the dichroic splits the light between the VIS and NIR arms. We also exclude the regions between the $J - H$ and $H - K$ bands which are strongly affected by telluric absorption. HyperZ also allows us to determine the best-fitting reddening as an additional parameter. Here we use a starburst galaxy extinction curve (Calzetti et al. 2000) as input. We do not constrain the reddening with that determined from the Balmer decrements where available (see Section 5.2), because the stars may not experience the same amount of reddening as the gas. For starburst galaxies, Calzetti (2001) finds that the radiation from stars and ionized gas experience different extinctions and that the stellar reddening is on the average 44 per cent of that in the gas phase. The flux attenuation bluewards of Lyα is taken into account using the prescription for the transmission in the intergalactic medium in Madau (1995).

For the galaxies with known spectroscopic redshifts, their redshifts are fixed in the template fitting, while in two cases (MACS 1115 and Abell 1689 ID 8.1), the best fit was also used to derive the photometric redshift. We do not constrain the template metallicities to the ones best matching the nebular abundances derived in Section 5.4, because these may not be the same, as older stellar populations, if present, may have lower metallicities reflecting the lower abundances of the gas at their time of formation. The output gives the best-fitting template which allows us to derive the ages, metallicities and reddening as listed in Table 14. The best-fitting spectra are overplotted in Fig. 2. One of the outputs of HyperZ is a scaling factor b allowing the galaxy stellar mass to be derived:

$$M_* = b(1+z)\, 4\pi D_L^2 / L_{\odot,bol},$$

where $L_{\odot,bol}$ is the solar bolometric luminosity (3.826×10^{33} erg s^{-1}) and D_L is the luminosity distance, where we assume a flat cosmology with $\Omega_\Lambda = 0.72$ and $H_0 = 73$ km s^{-1} Mpc^{-1}. The derived stellar mass is magnification dependent and is sensitive to slit losses. Table 14 lists the corrected stellar masses including the correction factors in Table 3. Uncertainties for the parameters (mass, age, reddening) are determined by adding to the initial spectrum the error spectrum multiplied by a random number normalized to a Gaussian distribution with $\sigma = 1$. A thousand fits are performed for each galaxy spectrum, and the standard deviations of the fitted values are taken as the uncertainties for the parameters.

In all cases the best-fitting templates are obtained with a model of an instantaneous burst of star formation. Such models are artificial in the sense that this would mean that there is no current on-going star formation, which is not correct because the galaxies show strong emission lines. Other templates that produce acceptable fits are those

Table 14. Best spectral fit parameters from Section 4.1. The masses, SFRs and magnitudes are corrected for slit losses and lens magnification factors.

Arc	$Z/Z_\odot$	Age (Myr)	$E(B-V)_{\rm stars}$ (mag)	$\log M_*$ ($M_\odot$)	UV SFR ($M_\odot\,{\rm yr}^{-1}$)	UV SSFR ($\rm Gyr^{-1}$)
A4.1	0.2	4 ± 3	0.10 ± 0.02	6.97 ± 0.08	0.4 ± 0.1	40 ± 11
A8.1	0.2	4 ± 3	0.07 ± 0.08	7.85 ± 0.15	1.6 ± 0.7	23 ± 11
A9.1	1.0	90 ± 50	0.00 ± 0.02	9.79 ± 0.13	0.6 ± 0.2	0.09 ± 0.04
A31.1	0.2	4 ± 2	0.17 ± 0.04	7.70 ± 0.10	1.0 ± 0.2	20 ± 6
M0304	0.4	57 ± 6	0.17 ± 0.02	10.57 ± 0.08	11.6 ± 2.3	0.30 ± 0.02
M0359	0.4	110 ± 18	0.15 ± 0.03	9.62 ± 0.13	1.5 ± 0.5	0.36 ± 0.05
M0416	1.0	32 ± 14	0.00 ± 0.08	8.70 ± 0.16	0.9 ± 0.2	1.8 ± 0.8
M1115	1.0	400 ± 260	0.00 ± 0.06	7.83 ± 0.22	0.007 ± 0.003	0.10 ± 0.06
M1206	1.0	20 ± 13	0.00 ± 0.03	9.23 ± 0.25	3.7 ± 0.6	2.2 ± 1.7
M1311	1.0	140 ± 20	0.15 ± 0.09	9.14 ± 0.21	0.3 ± 0.2	0.2 ± 0.1
M2031	0.2	4 ± 3	0.00 ± 0.03	9.16 ± 0.21	18.0 ± 8.2	13 ± 6
M2129	1.0	4700 ± 1500	0.07 ± 0.06	11.39 ± 0.12	0.003 ± 0.001	10^{-5}

with a small value of $\tau = 10$ Myr, while in a few cases, templates extracted from a constant SFR is also a valid solution. In a few cases, an exponentially increasing SFR also produces an acceptable fit. With these alternative fits the stellar masses remain the same as those listed in Table 14 to within ±10–20 per cent uncertainty.

As usually the case for SED fitting, there is a strong degeneracy between the age of the stellar population and the reddening. For any given spectrum, a similar good fit can be obtained with a younger population combined with more reddening of the template. The galaxy ages as obtained by the best fits are generally small ($\lesssim$100 Myr), and the reddenings are small as well, such that the allowed parameter space of reddening–age values is limited. One concern is that, if the ages are underestimated by the SED fit, the stellar masses will be as well. It is common in the literature to only include templates in the SED fits that are older than the typical dynamical time-scale for galaxies, i.e. older than a few 10 Myr (e.g. Wuyts et al. 2012b). For the lensed galaxies in this study, the resulting fits when forcing the age to be older than 20 Myr, the fits deteriorate significantly bluewards of the Lyα wavelengths. Similarly, if we fit the spectra with templates of a constant SFR and a lower limit for the age of a few times 10 Myr, the fits at UV wavelengths deteriorate, while the rest of the spectrum can be fitted well with an older template. We therefore choose to not constrain the possible template ages in the fitting. Another issue is that an underlying older stellar population can add to the total stellar mass, while not be detected because it does not contribute significantly to the UV radiation. Since the K-band fluxes of the galaxies are small, we argue that a significantly more massive older stellar population is not present. To better constrain the exact masses of an underlying older stellar populations in the galaxies, deep rest-frame NIR images are needed to fit the SED with a larger wavelength range.

4.2 Absolute magnitudes

A relevant question to ask given the heterogeneous sample, is what their magnitudes are relative to a typical galaxy at the same redshift. To calculate this, we use the best-fitting model spectrum to derive the magnitudes at rest frame 1500 Å, and compare these to the values of $M^*_{\rm AB}$, which depends on the redshift (Arnouts et al. 2005). We use the best-fitting templates, rather than the observed spectra because of the low S/N in the spectra. The resulting absolute magnitudes and that compared with $M^*_{\rm AB}(z)$ are listed in Table 15. The errors reflect the uncertainties in the magnification factor and slit losses.

For the galaxies with a low UV-flux characteristic for an evolved stellar population, neither their UV absolute magnitude nor their UV SFRs derived in Section 5.5 are relevant for comparing with star-forming galaxies at a given redshift selected in a uniform way from large surveys. When the spectra show evidence for older stellar populations it is more reasonable to compare the relative luminosities at rest-frame visual wavelengths. Table 15 lists the absolute magnitudes and luminosities of the galaxies at rest frame 6500 Å corrected for magnification and slit losses. Again the best-fitting template is used to determine the luminosities. For the Abell 1689 targets with poor NIR spectra, and M2031 at $z = 3.5$, the 6500 Å flux is based on the best-fitting template spectra at wavelengths redwards of the measured spectrum. The redshift-dependent characteristic magnitudes ($M^*_{\rm AB}$) defined by the luminosity function of galaxies in the rest-frame r' band are adopted from Gabasch et al. (2006).

Comparing the relative rest-frame UV and optical luminosities, we see that most galaxies are UV bright. This is by selection, since the observations targeted galaxies with both high total brightness and high surface brightness regions, which at higher redshifts implies a high UV surface brightness. The only exception in our sample is the M2129 arc, which was known to be an old evolved system based on its red colour and its morphology.

5 PHYSICAL CONDITIONS FROM EMISSION LINES

In this section we present properties of the lensed galaxies, which have sufficiently bright emission lines for a derivation of physical quantities. Diverse characteristics of the galaxies are expected, because the galaxies are not selected with a known redshift, nor appearance, hence we cannot derive a uniform set of properties for all sources with the current data set. All the physical properties derived in this section are summarized in Table 16. When line ratios are considered, we do not apply any correction for slit losses and magnification factors, since we assume that the emission lines come from the exact same region.

5.1 Kinematics

5.1.1 Line widths

We derive the mean velocity dispersion (σ) from all the emission-line widths, excluding Lyα when detected, and weighted with their

Table 15. Rest-frame optical absolute magnitudes and relative luminosities at 1500 and 6500 Å.

Arc	$M_{\rm AB,1500}$	$L/L^*(z, 1500\,\text{Å})$	$M_{\rm AB,6500}$	$L/L^*(z, 6500\,\text{Å})$
A4.1	-18.39 ± 0.29	0.2 ± 0.1	-17.93 ± 0.29	0.013 ± 0.004
A8.1	-20.56 ± 0.42	0.9 ± 0.4	-19.95 ± 0.42	0.07 ± 0.03
A9.1	-19.97 ± 0.41	0.5 ± 0.2	-23.81 ± 0.41	2.4 ± 1.0
A31.1	-19.76 ± 0.19	0.4 ± 0.1	-17.62 ± 0.19	0.008 ± 0.001
M0304	-22.46 ± 0.20	5.0 ± 1.0	-23.44 ± 0.20	1.7 ± 0.3
M0359	-19.82 ± 0.35	0.8 ± 0.3	-21.42 ± 0.35	0.3 ± 0.1
M0416	-19.65 ± 0.19	0.4 ± 0.1	-20.60 ± 0.19	0.1 ± 0.02
M1115	-13.65 ± 0.40	0.004 ± 0.002	-16.43 ± 0.40	0.004 ± 0.002
M1206	-21.55 ± 0.16	1.7 ± 0.3	-21.50 ± 0.16	0.24 ± 0.04
M1311	-18.22 ± 0.72	0.2 ± 0.1	-19.95 ± 0.72	0.08 ± 0.06
M2031	-23.39 ± 0.45	9.3 ± 4.2	-23.00 ± 0.45	1.0 ± 0.4
M2129	-13.28 ± 0.29	0.002 ± 0.001	-22.07 ± 0.29	0.8 ± 0.2

Table 16. Physical properties of sources with emission lines.

Arc	A4.1	A31.1	M0304	M0359	M0416	M1311	M2031	Section
Velocity dispersion σ (km s^{-1})	17 ± 1	22 ± 2	56 ± 1	53 ± 2	65 ± 9	53 ± 3	43 ± 1	5.1.1
ΔV ($z_{\rm em} - z_{\rm abs}$) (km s^{-1})	–	95 ± 131	-10 ± 55	–	–	–	80 ± 90	5.1.2
SFR([O II]) ($\text{M}_\odot\ \text{yr}^{-1}$)	0.7 ± 0.1	1.8 ± 0.3	55 ± 11	8.1 ± 2.7	4.7 ± 0.7	3.0 ± 1.8	7.1 ± 3.3	5.5
SFR(Hα)	0.4 ± 0.1	–	16 ± 3	1.5 ± 0.5	–	–	14.5 ± 6.5	
$E(B-V)_{\rm gas}$ (mag)	0.24 ± 0.13	0.37 ± 0.28	0.23 ± 0.01	0.29 ± 0.01	–	–	0.03 ± 0.33	5.2
log U	-2.7	-2.1	-2.8	-3.1	-2.4	-3.1	-2.1	5.3
log R_{23}	0.81 ± 0.04	0.85 ± 0.05	0.94 ± 0.001	0.67 ± 0.01	0.81 ± 0.04	0.19 ± 0.06	0.91 ± 0.02	5.4
12+log(O/H) (upper branch)	$\mathbf{8.33 \pm 0.08}$	8.45 ± 0.04	8.22 ± 0.01	$\mathbf{8.18 \pm 0.05}$	$\mathbf{8.44 \pm 0.06}$	$\mathbf{8.66 \pm 0.14}$	8.39 ± 0.01	5.4
12+log(O/H) (lower branch)	7.91 ± 0.11	$\mathbf{7.63 \pm 0.10}$	$\mathbf{8.16 \pm 0.01}$	7.48 ± 0.04	7.73 ± 0.11	7.13 ± 0.01	$\mathbf{7.74 \pm 0.03}$	
$Z/Z_\odot$ (lower; upper)	0.2; **0.4**	**0.1**; 0.6	**0.3**; 0.6	0.3; **0.3**	0.1; **0.3**	0.03; **0.9**	**0.1**; 0.5	
12+log(O/H) (*O3N2*)	–	–	8.04 ± 0.01	8.48 ± 0.01	–	–	–	
12+log(O/H) (*Ne3O2*)	8.24 ± 0.07	7.85 ± 0.15	8.20 ± 0.01	–	–	–	7.56 ± 0.11	

Notes. The listed SFRs assume a Chabrier IMF as described in the text. For completeness we list both the upper and the lower branch calibrations for the R_{23} diagnostics. The values in bold face represent the preferred values based on the ratios of either [Ne III]/[O II] or [O III]/[O II].

associated uncertainties. The measured line widths are corrected for instrumental resolution by measuring the widths of nearby unblended sky lines, and subtracting the widths in quadrature. The results are listed in Table 16. To determine the dynamical masses of the galaxies, their sizes need to be measured after lens modelling and source reconstruction, and will be presented elsewhere (Richard, in preparation). Although not included in Table 16 because only few lines are detected, we can still determine the velocity dispersion of the emission lines from M2129 ID 1.5 to be $147 \pm 17\,\text{km s}^{-1}$, and $40 \pm 3\,\text{km s}^{-1}$ for M1206 ID 2.1. The small velocity dispersions derived from the emission lines agree with the small stellar masses determined from the SED fits.

5.1.2 *Velocity offsets*

High-redshift galaxies show velocity offsets between Lyα emission and absorption lines, which are generally interpreted as galaxy scale outflows caused by feedback from star formation. Detailed studies have used the Lyα line to measure the emission-line redshift in comparison to rest-frame UV absorption lines arising in the ISM of the LBGs and found relative offsets of several $100\,\text{km s}^{-1}$ (Shapley et al. 2003), but also fainter galaxies identified by GRBs appear to have large velocity shifts (Milvang-Jensen et al. 2012). In a sample of eight Lyα-selected galaxies velocity offsets of $145^{+45}_{-23}\,\text{km s}^{-1}$ between the systemic redshifts from rest-frame optical emission lines and the Lyα lines have been measured (Hashimoto et al. 2012). These small velocity offsets are similar to the offsets determined from the two Lyα-emitting galaxies in this study. Since in the reference frame of the outflowing gas, photons bluewards of the Lyα line centre are shifted into resonance, the photons escape only after having diffused to the red wing. Verhamme, Schaerer & Maselli (2006) find that Lyα experiences about twice the velocity shift of the true outflow velocity in low hydrogen column density LBGs.

Some Lyα lines have a prominent blue cut-off in the spectral profile while others show both a blue and a much stronger red component. Observed at lower spectral resolution, the intrinsic redshift of the Lyα lines is difficult to determine. A better approach is to compare the ISM lines with other emission lines than Lyα, preferably measured with the same instrument to avoid systematic offsets. X-shooter spectra of the 8 o'clock arc show that the UV absorption lines and optical emission lines have redshifts consistent with each other (Dessauges-Zavadsky et al. 2011), but since the broad ISM absorption lines span a range of velocities relative to the systemic one, a galaxy scale outflow of $120\,\text{km s}^{-1}$ is likely. When outflows have been observed in galaxies, their ISM absorption lines are blueshifted with respect to the systemic redshift.

Table 4 lists both redshifts derived from emission and absorption lines. The absorption line redshifts are measured by fitting Gaussian functions and are less accurate because the S/N per pixel is low. Only for the sources with the brightest UV continuum can we measure reliably the redshifts from absorption lines. Even though the continuum is relatively bright, we find no significant ISM lines in the M0359 spectrum since at $z = 1.0$ most strong lines are bluewards

of the UVB spectrum. Strong low-ionization lines that are relatively easily detected and are not blended include Si II λ1260, Si II λ1304, C II λ1334 and Si II λ1526, and among the high-ionization species we detect S IV λλ1393, 1402 and C IV λλ1548, 1550. LBG spectra show velocity offsets between high- and low-ionization lines (Shapley et al. 2003), as well as offsets between emission and absorption lines indicative of galaxy scale outflows. Only in M0304 do we detect several high- and low-ionization species, but we do not detect any offset in velocity between the lines.

To determine if velocity offsets are seen in our sample, we list in Table 16 the velocity offsets derived from the difference between the average emission and absorption redshifts. When the velocity offset is positive, one can interpret this as an outflow. Within the errors, there is no evidence for large velocity offsets in our data. A more detailed study would require higher S/N data in particular to study the widths of the ISM lines. As the outflows in LBGs are driven by feedback from star formation, the lower SFRs in our galaxies relative to LBGs could result in smaller velocity offsets. In contrast, in low-mass galaxies which have weaker potential fields even small SFRs can drive a stronger wind. In such cases, the specific SFR (SSFR) is expected to correlate with the wind strengths as seen in $z \approx 1$ galaxies (Kornei et al. 2012).

5.2 Gas phase reddening

For five sources, more than one of the Balmer lines are detected and their flux ratios can be used to derive the gas phase reddening. As the ratios of emission lines are not affected by lens magnification and slit losses, we do not include those parameters in the calculations. The expected emission-line ratio in the absence of reddening is a function of the gas temperatures and densities. We adopt the values tabulated for temperatures $T = 10\,000$–$20\,000$ K and densities $n \sim 100\,\mathrm{cm}^{-3}$ in Brocklehurst (1971). The electron density of the gas in the lensed galaxies can be determined from the flux ratio of the [O II] λλ3727, 3730 doublet. The ratios of the lines are consistent with a low electron density $<300\,\mathrm{cm}^{-3}$ in all cases.

To derive the gas phase reddening, $E(B-V)_{\rm gas}$, we use all of the Balmer line pairs available for each of the galaxies and use a weighted average to determine the reddening. In practise this implies that the reddening is determined by the Balmer line ratio with the smallest uncertainty. We assume a starburst extinction curve (Calzetti et al. 2000), and list the resulting reddening in Table 16. The reddening derived for M2031 is very uncertain, but consistent with zero which was also found in the SED analysis in Section 4.1.

In the following analyses, all the emission-lines fluxes in Tables 5–13 are corrected for the intrinsic reddening $E(B-V)_{\rm gas}$, while for those galaxies where we do not constrain this parameter from emission-line ratios we use instead the reddening measured for the stars in Table 14, and assume a conversion to the reddening in the gas phase $E(B-V)_{\rm gas} = E(B-V)_{\rm stars}/0.44$ (Calzetti et al. 2000). Fig. 6 shows the reddening in the gas phase as a function of the reddening of the stars determined from SED fitting. The dashed line represents the scaling factor of 0.44 from Calzetti et al. (2000), which appears to be valid for the lensed galaxies as well.

5.3 Starburst or AGN ionization

The ionizing radiation from either active galactic nuclei (AGN) or recent star formation gives rise to strong emission lines in galaxies. Whether the emission is caused by an AGN rather than strong starbursts is usually investigated through emission-line ratios, which are sensitive to the hard ionization from AGN. Conventionally,

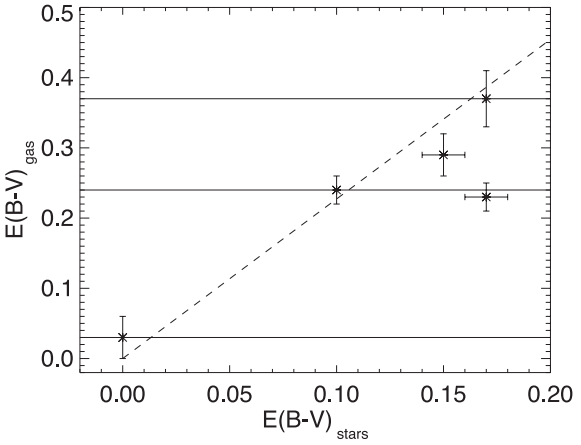

Figure 6. Reddening in the gas phase as a function of the stellar reddening determined from the SED fitting. The dashed line shows $E(B-V)_{\rm gas} = E(B-V)_{\rm stars}/0.44$ from Calzetti et al. (2000).

when only the strongest rest-frame optical emission lines can be detected in high-redshift galaxies, the line ratios [O III]/Hβ versus [N II]/Hα (Kewley & Dopita 2002) can be used. However, in our sample all these strong lines are only detected in M0304 and M0359. Both these galaxies have line ratios characteristic of star-forming galaxies.

In M2031, the C IV λλ1548, 1550 lines are not detected to a level of 3×10^{-18} erg cm^{-2} s^{-1}, so the ratio C IV/C III] < 0.15 indicates a softer ionizing spectrum, while an AGN would result in a fraction of 2 as argued for the Lynx arc (Binette et al. 2003). The line ratio for A31.1 is C IV/[C III,C III] $= 0.65 \pm 0.71$ indicating a higher ionization parameter. In AGN, the lines N V λλ1238, 1242 and He II λ1640 are expected to be strong, and since these lines are not detected in any of your spectra it suggests that the main contributor to the ionization is massive stars.

With the numerous emission lines detected from the sources it is possible to derive the ionization parameter, U, for the galaxies. We use the [O III] λλ4959, 5007/[O II] λλ3727, 3730 combined with the oxygen abundances to calculate log U using the iterative calculations in Kewley & Dopita (2002). The resulting values lie in the range between -3 and -2, which is higher than measured in local galaxies, but typical for high-redshift galaxies, both unlensed (Erb et al. 2006, 2010) and lensed ones (Hainline et al. 2009; Richard et al. 2011a; Rigby et al. 2011).

5.4 Oxygen abundance

Oxygen abundances can be determined from the strong rest-frame optical emission lines. These values are not magnification dependent, because the parameters are derived based on line flux ratios rather than absolute values. A more accurate method to determine abundances rely on the detection of temperature-sensitive emission lines which are typically faint and very rarely detected in high-redshift galaxies. In three of the lensed galaxies at $2 < z < 3.5$, the temperature-sensitive ratios of [O III] λ5007 and the O III] λλ1661, 1666 doublet allow us to use the direct $T_{\rm e}$ methods, which is presented in Christensen et al. (2012).

When the temperature-sensitive lines are absent from the spectra, one has to rely on the relations between strong emission-line ratios and the oxygen abundances calibrated from direct $T_{\rm e}$ methods (Osterbrock 1989). The ratio defined as R_{23} = ([O II] λλ3727, 3730+[O III] λλ4959, 5007)/Hβ introduced by Pagel et al. (1979) is

one of the most used calibrations, since the relevant emission lines are detectable from ground-based data out to $z = 3.8$. However, the R_{23} relation has two possible solutions with a high-metallicity and a low-metallicity branch. A wealth of authors have published separate calibrations of the R_{23} diagnostics based either on photoionization models (e.g. McGaugh 1991; Kobulnicky, Kennicutt & Pizagno 1999; Kewley & Dopita 2002) or direct calibrations derived from temperature-sensitive lines (e.g. Alloin et al. 1979; Pilyugin & Thuan 2005; Nagao, Maiolino & Marconi 2006). Typically, these calibrations posses an intrinsic scatter of ∼0.2 dex, and in absolute terms various calibrations may differ by up to 0.7 dex relative to each other (Kewley & Ellison 2008).

A degenerate solution can be avoided if other emission lines such as [N II] λ6586 or [Ne III] λ3869 are detected (Denicoló, Terlevich & Terlevich 2002; Kewley & Dopita 2002; Pettini & Pagel 2004; Liang et al. 2006). Also the [O III]5007/[O II]3727 ratio can be used to discriminate between the upper and lower branch of the calibration (Nagao et al. 2006). We detect [N II] λ6586 in two of the spectra, while [Ne III] λ3869 is detected in three galaxies. For seven sources we can determine the R_{23} ratio, including those with direct oxygen abundance determinations (Christensen et al. 2012).

For the A4.1 source, the Hγ flux is scaled to determine Hβ. Its Hα to Hγ ratio suggests a reddening of $E(B-V) = 0.24 \pm 0.13$, so correcting Hα for the intrinsic extinction, and given that Hβ is a factor of 2.86 fainter than Hα we derive a corrected Hβ flux of $(37.6 \pm 3.2) \times 10^{-18}$ erg cm^{-2} s^{-1}. The other emission lines are also corrected for this reddening value.

For some galaxies, [O III] λ4959 is not detected, noisier because of telluric absorption, or close to a sky emission line. In those cases, we use the relation $I5007 = 2.98 \times I4959$ to determine the total flux of the doublet (Storey & Zeippen 2000). To derive the oxygen abundance, we use the expression for the upper and lower branch of the R_{23} calibration in Pilyugin & Thuan (2005). The R_{23}, 12+log(O/H) values and the propagated errors are listed in Table 16. For completeness both the upper and lower branch abundances are listed. Gas phase abundances are derived relative to the solar value of 12+log(O/H) = 8.69 (Asplund et al. 2009). We can use the additional detected lines for some of the galaxies to constrain which of the upper or lower branch of the abundance calibration is valid. Following Cresci et al. (2012), we assume the upper R_{23} branch is valid for galaxies with log([O III]/[O II]) < 0.45 and log([Ne III]/[O II]) < 0.6. Whether the upper or lower branch is preferred is indicated by the oxygen abundances listed in bold face numbers in Table 16.

To justify further the choice of the upper or lower branch of the metallicity calibrations, Table 16 also lists the oxygen abundances using the *O3N2* calibration (Pettini & Pagel 2004) and *Ne3O2* calibration (Nagao et al. 2006). In all cases, these calibrations agree with the preferred branch of the R_{23} relation. The various oxygen abundance determinations vary within 0.3 dex, which illustrates well the known offset between various strong line calibrations (Kewley & Ellison 2008).

In the case of M2031, M0304 and Abell 1689 ID 31.1, all have direct abundances measurements (see Christensen et al. 2012) consistent with those inferred from the lower branch of the R_{23} calibration in Pilyugin & Thuan (2005).

5.5 Star formation rates

We determine the SFRs using three methods: [O II] and Hα emission lines, and the UV continuum flux at rest frame 1500–2800 Å. The measured emission-line fluxes are corrected for the slit losses and magnification factors (Table 3), and we also correct the fluxes for the intrinsic reddening. From the sum of the flux in the doublet [O II] λ3727, 3730 we calculate the extinction-corrected luminosity ($L_{[\mathrm{O\,II}],\mathrm{cor}}$ based on the gas phase reddening, $E(B-V)_{\mathrm{gas}}$), and use the relation in Kennicutt (1998) to derive the intrinsic SFR. We divide the conversion factor by 1.7 to correct the SFR from a Salpeter IMF to a Chabrier IMF. In a similar manner we calculate the SFR based on the Hα lines, which is detected for three of the galaxies. Again the SFR conversion is divided by a factor of 1.7. The resulting values are listed in Table 16. In addition, we also calculate the SFR from M2031 assuming that Hα is 2.86 times the Hβ flux in the case of a zero reddening. In the following Section 6, we use the SFRs based on the [O II] λλ3727, 3730 doublet. Once corrected for reddening, SFRs based on [O II] and Hα are generally in good agreement (e.g. Kewley, Geller & Jansen 2004), and Hα is known as a good tracer of the current ongoing SFR.

As an alternative, we also calculate the SFR from the rest-frame UV luminosity at 1500–2800 Å using the calibration in Kennicutt (1998), again correcting the scaling relation for the IMF difference by dividing by a factor 1.7. We make use of the best-fitting spectral models available for all of the galaxies in our sample, correct these for the reddening $E(B-V)_{\mathrm{stars}}$ and determine the UV flux at the rest-frame 1500 Å. The resulting SFRs are listed in Table 14.

The uncertainties for the SFRs are propagated and contain the uncertainties measured either for the [O II] flux or the UV continuum as well as the uncertainty for the slit loss and magnification factors. When two or more estimates of the SFRs can be derived, we find that the values are consistent to within a factor of 2. In contrast to the SFRs, the SSFRs, i.e. the SFRs divided by the stellar mass, do not depend on the magnification factor, slit losses or choice of IMF. The inverse of the SSFRs can be taken as the formation time-scale of the galaxy given that the SFR is constant. For a galaxy with a small SFR and high stellar masses, the correspondingly low SSFR suggests that the SFR must have been higher in the past. In particular, M2129, the oldest galaxy in our sample, shows evidence of only little present ongoing star formation. The [O II] λλ3727, 3730 doublet is detected at a level corresponding to a SFR $= 0.8\,\mathrm{M}_{\odot}\,\mathrm{yr}^{-1}$, implying that much stronger star formation has taken place in the past to build up the stellar mass in this massive galaxy.

6 FUNDAMENTAL RELATION FOR STAR-FORMING GALAXIES

6.1 Mass–metallicity relations

Observations of mass–metallicity relations have revealed an evolution with increasing redshifts from local galaxies in Sloan Digital Sky Survey (SDSS; Tremonti et al. 2004), field galaxies at $z = 0.7$ (Savaglio et al. 2005) and out to $z > 3$ (Maiolino et al. 2008; Mannucci et al. 2009). Richard et al. (2011a) analyse a larger sample of lensed galaxies at $1.5 < z < 3.3$, and find the galaxy metallicities at $z \sim 3$ are slightly larger than field galaxies.

Fig. 7 shows that the lensed galaxies exhibit a huge scatter compared to the established relations, and we do not find any clear correlation. The highest stellar mass galaxy, M0304, belongs to a merging system, and therefore naturally has a lower observed metallicity relative to the expected value from extrapolation of the mass–metallicity relations.

Since the mass–metallicity relations are based on various emission-line diagnostics, which exhibit offsets with respect to each other (Kewley & Ellison 2008), it is not straightforward to analyse the evolution of the mass–metallicity relation with redshift when

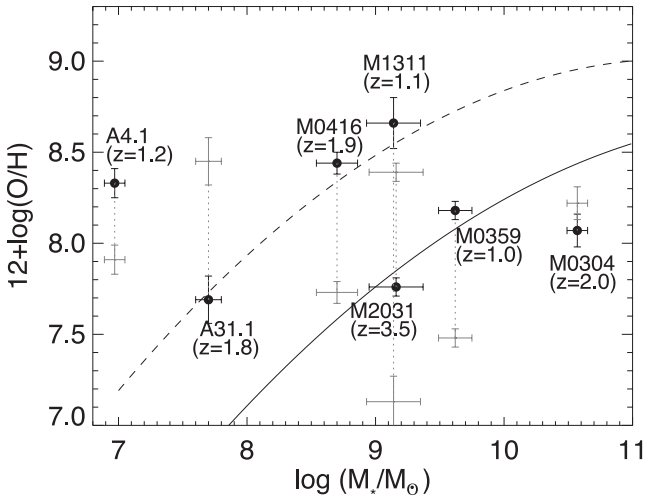

Figure 7. Oxygen abundances of the lensed galaxies as a function of the stellar masses, corrected for lens magnifications. The black circles show the oxygen abundances from the preferred branch of the R_{23} relation including the direct measurements for A31.1, M0304 and M2031, while the grey error bars show the location of the galaxies if the alternate branch of the R_{23} relation is adopted for all galaxies. The mass–metallicity relation for LBGs at $z = 3$–4 is shown by the solid line (Maiolino et al. 2008; Mannucci et al. 2009), and galaxies at $z = 0.7$ by the dashed line (Savaglio et al. 2005).

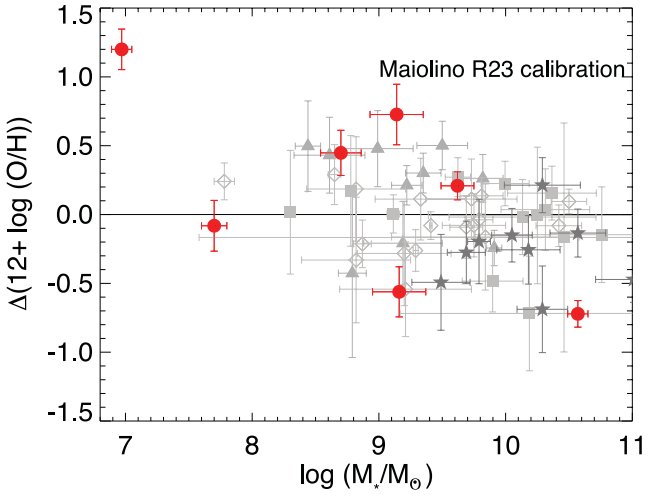

Figure 8. Offsets of the derived oxygen abundance compared to the predicted one from the fundamental relation in Mannucci et al. (2011). The red circles show the location of the preferred R_{23} branch with the calibration in Maiolino et al. (2008), and using the direct measurements for A31.1, M0304 and M2031 in Christensen et al. (2012). A location above zero implies that the measured metallicity is higher than expected from the relation. The grey squares show the offsets of 13 lensed galaxies at $z = 2$–3 for which either the R_{23} or the *N2* calibration from Maiolino et al. (2008) was used (Richard et al. 2011a). The grey triangles show offsets of 10 lensed galaxies at $z = 1$–2 in Wuyts et al. (2012b) for which the oxygen abundance was derived from the *N2* calibration in Maiolino et al. (2008). The outlined diamonds represent 18 GRB hosts at $z < 1$ (Mannucci et al. 2011), and the star symbols represent unlensed and more massive $z \sim 3.5$ galaxies (Maiolino et al. 2008).

different galaxy samples are involved. Such offsets in abundance diagnostics can partly explain the reason why the lensed galaxies do not follow any of the correlations at a given redshift.

6.2 Fundamental relation at low stellar masses

The fundamental relation between galaxies SFRs, oxygen abundances and stellar masses calibrated for low-redshift, high-mass galaxies (Lara-López et al. 2010; Mannucci et al. 2010) have revealed a larger scatter when extending relation to lower stellar masses. In particular, GRB host galaxies with $M_* \lesssim 10^9\,\mathrm{M}_\odot$ show a larger scatter relative to the fundamental relation (Kocevski & West 2011; Mannucci, Salvaterra & Campisi 2011), and Mannucci et al. (2011) provide an extension of the fundamental relation at lower stellar masses. Recent observations show that also a low stellar mass Type Ia supernova host galaxy at $z = 1.55$ follows this relation (Frederiksen et al. 2012).

If we calculate the differences between the oxygen abundances in Table 16 and the calibration in Mannucci et al. (2011), we find that the galaxies exhibit a large scatter compared to the relation. A potential risk when analysing and comparing abundances is that there is a significant offset between various emission-line diagnostics (Kewley & Ellison 2008). We therefore also derive the oxygen abundances using the calibrations in Maiolino et al. (2008), which correspond to the abundances used in the derivation of the fundamental relation in Mannucci et al. (2010). The offsets are illustrated in Fig. 8. Other low-mass lensed galaxies at $z = 1$–3 (Richard et al. 2011a; Wuyts et al. 2012b) illustrated by squares and triangles in Fig. 8 show a similar trend of not following the fundamental relation. The standard deviation of the offsets from the relation is 1 dex, and the galaxy with the lowest stellar mass, A4.1, is offset by ∼1 dex. In any case, the high abundance of this galaxy is unexpected given its low stellar masses. The basis of the selection of the upper branch for the R_{23} abundance calibration is that the flux ratios of [Ne III]/[O II] and [O III]/[O II] suggest a higher abundance (Nagao et al. 2006; Cresci et al. 2012).

In addition to the large scatter, the locations of the galaxies have a slope of $-0.3\,\mathrm{dex}^{-1}$ in $\log M_*$, which is statistically significant with a Spearman non-parametric correlation test giving a probability of 0.98. The calibration of the fundamental relation in Lara-López et al. (2010) also produces a slope and a large scatter.

Our finding of a discrepant location of the lensed galaxies compared to the fundamental relation for star-forming galaxies in Mannucci et al. (2010) and the extension to low-mass galaxies in Mannucci et al. (2011) does not imply that a fundamental relation is not present. It merely suggests that the scatter is significant when low-mass galaxies are analysed. Massive lensed galaxies analysed in the literature follow the fundamental relation when their metallicities are 12+log(O/H) > 8.0, and stellar masses larger than $10^{10}\,\mathrm{M}_\odot$ (Dessauges-Zavadsky et al. 2011; Richard et al. 2011a), while lensed galaxies with stellar masses below $\sim 10^{10}\,\mathrm{M}_\odot$ have in majority larger metallicity than expected from the fundamental relation (Richard et al. 2011a; Wuyts et al. 2012b) consistent with our findings.

If we assume that the oxygen abundance in the fundamental relation equation depends only on the SFR, the galaxies would fall within 0.5 dex of a relation. Similarly, a smaller scatter with respect to the fundamental relation can be obtained if the SFR is not included, and only the stellar mass is a dependent variable. However, the minimum scatter with respect to the relation is maintained with a combination of dependence of both the stellar mass and the SFR. Mannucci et al. (2010) define a projection of the fundamental relation: $\mu_\alpha = \log(M_*) - \alpha \log(\mathrm{SFR})$, where $\alpha = 0.32$ gives the smallest scatter. For the lensed galaxies with stellar masses below $10^{10}\,\mathrm{M}_\odot$, we determine the smallest scatter at $\alpha = 0.36$.

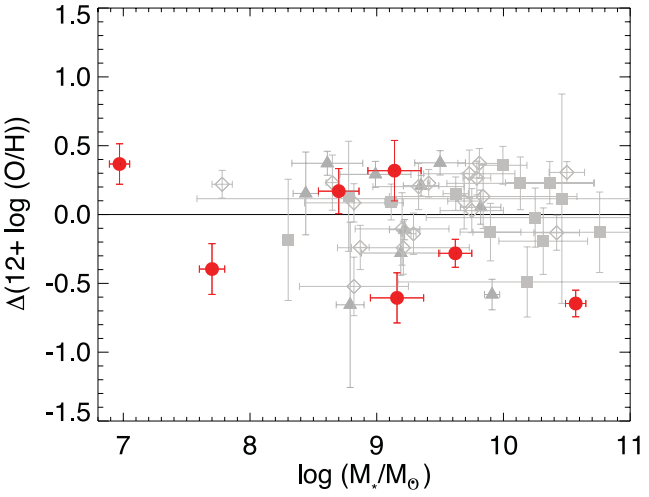

Figure 9. Offset in measured abundance compared to the new calibration of the fundamental relation given by equation (1). The symbols present the same data as in Fig. 8. From the entire sample of lensed galaxies combined with low-redshift GRB hosts, we measure a standard deviation of $\sigma = 0.3$ dex.

Since the sample of lensed galaxies is so small compared to the 140 000 SDSS galaxies, we can only suggest an alternative fit for the fundamental relation valid for low-mass galaxies. The oxygen abundances for all the lensed galaxies and the GRB hosts from Mannucci et al. (2011) are fitted with the functional form of the fundamental relation in Mannucci et al. (2010). The resulting fit is

$$12 + \log(\mathrm{O/H}) = 8.52 + 0.26m + 0.013s + 0.025m^2 - 0.026ms + 0.013s^2, \quad (1)$$

where $s = \log(\mathrm{SFR})$ and $m = \log(M_*) - 10$ in solar units. With this alternative calibration, the scatter is 0.3 dex and the slope is absent as demonstrated in Fig. 9. A Spearman test gives a probability of 0.3 for a correlation.

One concern is that the R_{23} calibration is not an accurate metallicity tracer given the large offsets between various strong line calibrations (Kewley & Ellison 2008). A comparison of the oxygen abundances from R_{23} and the direct T_e method for metal-rich, local SDSS galaxies suggests that the T_e-based log(O/H) abundances are lower by up to 0.6 dex compared to the upper branch of the R_{23} relation (Liang et al. 2007). However, for the galaxies in our sample we find that the R_{23} calibration in Pilyugin & Thuan (2005) is in agreement with direct T_e-based abundances for three of the galaxies (Christensen et al. 2012). For the other four galaxies we can only assume that this is valid too.

Since the lens magnification as well as the slit loss correction affects both the SFR and stellar masses equally, any uncertainty in the magnification factor and correction factor has little impact on the location of the galaxies relative to the fundamental relation. The only assumption is that the emission lines are uniformly distributed over the entire galaxy, such that the emission-line flux follows the continuum flux. Metallicity gradients are known to be present in disc galaxies, so we likely overestimate the integrated oxygen abundance slightly. Considering that gradients are typically a few times 0.1 dex over the face of a large (local) galaxy, and that the lensed galaxies in this study are compact sources dominated by at most a few luminous H II regions, any metallicity gradient cannot explain an integrated 1 dex offset relative to the fundamental relation.

7 DISCUSSION AND SUMMARY

We have presented spectroscopic data and determined redshifts for 12 strongly lensed galaxies behind various massive galaxy clusters. Three of the redshifts were previously determined by other studies. Although the selection of the lensed galaxies is based on optical data, and therefore makes a preferential selection of UV-bright high-redshift galaxies, we still achieve a sample of various galaxy properties (young and old, reddened and non-reddened, star forming and non-star forming), because we do not include colour selections. The lensing magnification effect allows us to carry out detailed investigations of galaxies that are on the average one to two orders of magnitude fainter and less massive than galaxies studied in unlensed field populations. The galaxies are also intrinsically fainter than other lensed galaxies studied in the literature, simply because we targeted galaxies with observed magnitudes ∼24, which is fainter than the ones investigated previously.

Using the stellar masses, SFRs and oxygen abundances, we find a breakdown of the fundamental relation for star-forming galaxies at very low stellar masses ($M < 10^{10}\,\mathrm{M}_\odot$) with offsets larger than 1 dex, which implies that one cannot use the calibration in Mannucci et al. (2010) to derive any missing parameter (SFR, M_* or oxygen abundance) when two other parameters are known for high-redshift galaxies. Contrary to the suggestion that the relation is not valid at $z > 2.5$, we find one galaxy at $z = 3.5$ with a metallicity only 0.4 ± 0.1 dex too low compared to the expectation from the fundamental relation. We provide an alternative calibration extending the low-mass end of the fundamental relation.

Our findings of the SFRs from various indicators (UV continuum versus either [O II] or Hα emission lines) agree with each other within a factor of 2 after correcting for the intrinsic reddening. Such spreads in the SFR estimates from various diagnostics are known for LBGs (Erb et al. 2003). However, Wuyts et al. (2012a) find that the SFRs after dust correction in four lensed $z = 2$ galaxies agree under the assumption that the extinction law is steeper than a Calzetti law as observed for unlensed LBGs (Reddy et al. 2010). In the lensed galaxies studied here, the UV-based SFRs are on the average lower than inferred from emission lines, which would support the suggestions of a steeper extinction curve, such that the UV flux should be corrected by a larger factor to match the SFRs based on emission lines. However, even if the SFRs are overestimated by a factor of 2, this would make no impact on the offset of the lensed galaxies with respect to the fundamental relations between the SFR, stellar mass and oxygen abundances explored in Section 6.

We find no evidence for velocity offsets between rest-frame UV and optical emission lines and UV absorption lines when both are detected, since the offsets we derive are only significant on the 1σ level. Observations of high-redshift galaxies have interpreted offsets between Lyα and UV absorption lines or optical emission lines as indication of galaxy outflows of up to several $100\,\mathrm{km\,s^{-1}}$, even though the velocity offset of Lyα emission lines can be explained by radiation transfer effect in expanding neutral gas without the need for extreme velocities. The combination of accurate redshift determination from intermediate-resolution spectra combined with a full spectral coverage is essential to investigate individual galaxies for these kinematic effects. High-velocity outflows from galaxies can also be inferred from the extension in velocity space of the ISM absorption lines, but in the low S/N spectra investigated here, we cannot determine if the absorption lines span a large velocity range.

One of the driving questions behind this investigation is which galaxies have strong emission lines that are detected with shallow spectra. Galaxies without bright knots (or equivalent to H II regions),

do not have strong emission lines. A8.1 and M1115 show no emission lines at all, while M1311 has only very faint lines. Abell 1689 ID 8.1 is a giant arc, which has a blue continuum suggesting a young galaxy with ongoing star formation. With a redshift $z = 2.68$, it should have detectable emission lines, also beyond Lyα. The Lyα line itself could easily be absorbed as it is only detected in about 25 per cent of LBGs. On the other hand, other lines could be present but just absorbed or obscured. As seen in the M1206 arc, we only detect a single but very strong emission line from [O III] λ5007, while all the other strong emission lines in the large wavelength range spanned by X-shooter fall behind strong sky emission lines, or absorbed by telluric lines. In the case of M1115, which is a low surface brightness arc, the photometric redshift is either low or high, so emission lines are expected. However, the SED of the galaxy suggests an old stellar population, where emission lines in H II regions are no longer produced.

Alternatively, we can compare the relative luminosities at the rest-frame UV and optical. Not surprisingly, the galaxies with low absolute UV luminosity relative to that in the rest frame (M1115 and M2129) do not exhibit strong emission lines. When comparing the rest-frame UV and optical luminosities in Table 15, most galaxies can be separated into UV bright or UV faint relative to their optical luminosities. We find that the galaxies without emission lines are those with fractional luminosities $L/L^*(\mathrm{UV}) \lesssim L/L^*(\mathrm{optical})$. The only exception is again A8.1.

In future studies when large numbers of gravitational lensed candidates are detected in multiband images covering large areas on the sky, we intend to focus not only on galaxies with obvious clumpy morphologies indicating the presence of H II regions and on-going star formation, but also on the galaxies with steep spectral slopes.

ACKNOWLEDGMENTS

The Dark Cosmology Centre is funded by the DNRF. LC acknowledges the support of the EU under a Marie Curie Intra-European Fellowship, contract PIEF-GA-2010-274117. JR is supported by the Marie Curie Career Integration Grant 294074. PL acknowledges funding from the Villum foundation. BM-J acknowledges support from the ERC-StG grant EGGS-278202. We thank Daniel Schaerer for discussions about HyperZ, and Roser Pelló for modifying HyperZ to allow the fitting of spectra. Thanks to Bram Venemans for discussions about X-shooter data reduction, and Stefano Covino, Valerio D'Elia, Johan P. U. Fynbo, Daniele Malesani, Hans Ulrik Nørgaard-Nielsen and Beate Stelzer for carrying out the observations. We also thank the anonymous referee for comments and suggestions that improved the presentation of the results.

REFERENCES

Abell G. O., Corwin H. G., Jr, Olowin R. P., 1989, ApJS, 70, 1
Allam S. S., Tucker D. L., Lin H., Diehl H. T., Annis J., Buckley-Geer E. J., Frieman J. A., 2007, ApJ, 662, L51
Alloin D., Collin-Souffrin S., Joly M., Vigroux L., 1979, A&A, 78, 200
Arnouts S. et al., 2005, ApJ, 619, L43
Asplund M., Grevesse N., Sauval A. J., Scott P., 2009, ARA&A, 47, 481
Bertin E., Arnouts S., 1996, A&AS, 117, 393
Bian F. et al., 2010, ApJ, 725, 1877
Binette L., Groves B., Villar-Martín M., Fosbury R. A. E., Axon D. J., 2003, A&A, 405, 975
Bohlin R. C., Dickinson M. E., Calzetti D., 2001, AJ, 122, 2118
Bolzonella M., Miralles J.-M., Pelló R., 2000, A&A, 363, 476
Bradley L. D. et al., 2008, ApJ, 678, 647
Bristow P., Kerber F., Rosa M. R., Vernet J., Goldoni P., Spanò P., Modigliani A., 2008, Proc. SPIE, 7014, 128
Broadhurst T. et al., 2005, ApJ, 621, 53
Brocklehurst M., 1971, MNRAS, 153, 471
Bruzual G., Charlot S., 2003, MNRAS, 344, 1000
Cabanac R. A., Valls-Gabaud D., Jaunsen A. O., Lidman C., Jerjen H., 2005, A&A, 436, L21
Cabanac R. A., Valls-Gabaud D., Lidman C., 2008, MNRAS, 386, 2065
Calzetti D., 2001, PASP, 113, 1449
Calzetti D., Armus L., Bohlin R. C., Kinney A. L., Koornneef J., Storchi-Bergmann T., 2000, ApJ, 533, 682
Chabrier G., 2003, PASP, 115, 763
Christensen L., D'Odorico S., Pettini M., Belokurov V., Evans N. W., Kellogg M., Vernet J., 2010, MNRAS, 406, 2616
Christensen L., Richard J., Hjorth J., Laursen P., Milvang-Jensen B., Dessauges-Zavadsky M., Grillo C., Ebeling H., 2012, MNRAS, 427, 1973 (this issue)
Cresci G., Mannucci F., Sommariva V., Maiolino R., Marconi A., Brusa M., 2012, MNRAS, 421, 262
Denicoló G., Terlevich R., Terlevich E., 2002, MNRAS, 330, 69
Dessauges-Zavadsky M., D'Odorico S., Schaerer D., Modigliani A., Tapken C., Vernet J., 2010, A&A, 510, A26
Dessauges-Zavadsky M., Christensen L., D'Odorico S., Schaerer D., Richard J., 2011, A&A, 533, A15
Diehl H. T. et al., 2009, ApJ, 707, 686
D'Odorico S. et al., 2006, Proc. SPIE, 6269, 98
Ebeling H., Edge A. C., Henry J. P., 2001, ApJ, 553, 668
Ebeling H., Barrett E., Donovan D., Ma C.-J., Edge A. C., van Speybroeck L., 2007, ApJ, 661, L33
Ebeling H., Ma C. J., Kneib J., Jullo E., Courtney N. J. D., Barrett E., Edge A. C., Le Borgne J., 2009, MNRAS, 395, 1213
Ebeling H., Edge A. C., Mantz A., Barrett E., Henry J. P., Ma C. J., van Speybroeck L., 2010, MNRAS, 407, 83
Erb D. K., Shapley A. E., Steidel C. C., Pettini M., Adelberger K. L., Hunt M. P., Moorwood A. F. M., Cuby J.-G., 2003, ApJ, 591, 101
Erb D. K., Shapley A. E., Pettini M., Steidel C. C., Reddy N. A., Adelberger K. L., 2006, ApJ, 644, 813
Erb D. K., Pettini M., Shapley A. E., Steidel C. C., Law D. R., Reddy N. A., 2010, ApJ, 719, 1168
Fosbury R. A. E. et al., 2003, ApJ, 596, 797
Frederiksen T., Hjorth J., Maund J. R., Rodney S. A., Riess A. G., Dahlen T., Mobasher B., 2012, ApJ, in press (arXiv:1210.3053)
Fynbo J. P. U., Ledoux C., Møller P., Thomsen B., Burud I., 2003, A&A, 407, 147
Gabasch A. et al., 2006, A&A, 448, 101
Goldoni P., Royer F., François P., Horrobin M., Blanc G., Vernet J., Modigliani A., Larsen J., 2006, Proc. SPIE, 6269, 80
Grillo C., Christensen L., 2011, MNRAS, 418, 929
Hainline K. N., Shapley A. E., Kornei K. A., Pettini M., Buckley-Geer E., Allam S. S., Tucker D. L., 2009, ApJ, 701, 52
Halkola A., Seitz S., Pannella M., 2006, MNRAS, 372, 1425
Hashimoto T., Ouchi M., Shimasaku K., Ono Y., Nakajima K., Rauch M., Lee J., Okamura S., 2012, arXiv e-prints (arXiv:1206.2316)
Hjorth J. et al., 2012, ApJ, 756, 187
Jullo E., Kneib J.-P., Limousin M., Elíasdóttir Á., Marshall P. J., Verdugo T., 2007, New J. Phys., 9, 447
Jullo E., Natarajan P., Kneib J., D'Aloisio A., Limousin M., Richard J., Schimd C., 2010, Sci, 329, 924
Kennicutt R. C., 1998, ARA&A, 36, 189
Kewley L. J., Dopita M. A., 2002, ApJS, 142, 35
Kewley L. J., Ellison S. L., 2008, ApJ, 681, 1183
Kewley L. J., Geller M. J., Jansen R. A., 2004, AJ, 127, 2002
Kobulnicky H. A., Kennicutt R. C., Jr, Pizagno J. L., 1999, ApJ, 514, 544
Kocevski D., West A. A., 2011, ApJ, 735, L8
Kornei K. A., Shapley A. E., Martin C. L., Coil A. L., Lotz J. M., Schiminovich D., Bundy K., Noeske K. G., 2012, ApJ, 758, 135
Krühler T. et al., 2012, ApJ, 758, 46
Lara-López M. A. et al., 2010, A&A, 521, L53

Liang Y. C., Yin S. Y., Hammer F., Deng L. C., Flores H., Zhang B., 2006, ApJ, 652, 257
Liang Y. C., Hammer F., Yin S. Y., Flores H., Rodrigues M., Yang Y. B., 2007, A&A, 473, 411
Limousin M. et al., 2007, ApJ, 668, 643
Lin H. et al., 2009, ApJ, 699, 1242
McGaugh S. S., 1991, ApJ, 380, 140
Madau P., 1995, ApJ, 441, 18
Maiolino R. et al., 2008, A&A, 488, 463
Mannucci F. et al., 2009, MNRAS, 398, 1915
Mannucci F., Cresci G., Maiolino R., Marconi A., Gnerucci A., 2010, MNRAS, 408, 2115
Mannucci F., Salvaterra R., Campisi M. A., 2011, MNRAS, 414, 1263
Milvang-Jensen B., Fynbo J. P. U., Malesani D., Hjorth J., Jakobsson P., Møller P., 2012, ApJ, 756, 25
Modigliani A. et al., 2010, Proc. SPIE, 7737, 56
Nagao T., Maiolino R., Marconi A., 2006, A&A, 459, 85
Nilsson K. K., Östlin G., Møller P., Möller-Nilsson O., Tapken C., Freudling W., Fynbo J. P. U., 2011, A&A, 529, A9
Osterbrock D. E., 1989, Astrophysics of Gaseous Nebulae and Active Galactic Nuclei. University Science Books, Mill Valley, CA
Pagel B. E. J., Edmunds M. G., Blackwell D. E., Chun M. S., Smith G., 1979, MNRAS, 189, 95
Patat F. et al., 2011, A&A, 527, A91
Pettini M., Pagel B. E. J., 2004, MNRAS, 348, L59
Pettini M., Steidel C. C., Adelberger K. L., Dickinson M., Giavalisco M., 2000, ApJ, 528, 96
Pettini M., Rix S. A., Steidel C. C., Adelberger K. L., Hunt M. P., Shapley A. E., 2002, ApJ, 569, 742
Pettini M. et al., 2010, MNRAS, 402, 2335
Pilyugin L. S., Thuan T. X., 2005, ApJ, 631, 231
Postman M. et al., 2012, ApJS, 199, 25
Quider A. M., Pettini M., Shapley A. E., Steidel C. C., 2009, MNRAS, 398, 1263
Quider A. M., Shapley A. E., Pettini M., Steidel C. C., Stark D. P., 2010, MNRAS, 402, 1467
Reddy N. A., Erb D. K., Pettini M., Steidel C. C., Shapley A. E., 2010, ApJ, 712, 1070
Richard J. et al., 2010, MNRAS, 404, 325
Richard J., Jones T., Ellis R., Stark D. P., Livermore R., Swinbank M., 2011a, MNRAS, 413, 643
Richard J., Kneib J.-P., Ebeling H., Stark D. P., Egami E., Fiedler A. K., 2011b, MNRAS, 414, L31
Rigby J. R., Wuyts E., Gladders M. D., Sharon K., Becker G. D., 2011, ApJ, 732, 59
Salpeter E. E., 1955, ApJ, 121, 161
Savaglio S. et al., 2005, ApJ, 635, 260
Schlegel D. J., Finkbeiner D. P., Davis M., 1998, ApJ, 500, 525
Shapley A. E., Steidel C. C., Pettini M., Adelberger K. L., 2003, ApJ, 588, 65
Stark D. P., Swinbank A. M., Ellis R. S., Dye S., Smail I. R., Richard J., 2008, Nat, 455, 775
Storey P. J., Zeippen C. J., 2000, MNRAS, 312, 813
Swinbank A. M., Bower R. G., Smith G. P., Wilman R. J., Smail I., Ellis R. S., Morris S. L., Kneib J.-P., 2007, MNRAS, 376, 479
Teplitz H. I. et al., 2000, ApJ, 533, L65
Tremonti C. A. et al., 2004, ApJ, 613, 898
van Dokkum P. G., 2001, PASP, 113, 1420
Verhamme A., Schaerer D., Maselli A., 2006, A&A, 460, 397
Vernet J. et al., 2008, Proc. SPIE, 7016, 46
Vernet J. et al., 2011, A&A, 536, A105
Villar-Martín M., Cerviño M., González Delgado R. M., 2004, MNRAS, 355, 1132
Wuyts E., Rigby J. R., Gladders M. D., Gilbank D. G., Sharon K., Gralla M. B., Bayliss M. B., 2012a, ApJ, 745, 86
Wuyts E., Rigby J. R., Sharon K., Gladders M. D., 2012b, ApJ, 755, 73
Yuan T., Kewley L. J., 2009, ApJ, 699, L161
Zitrin A., Broadhurst T., Barkana R., Rephaeli Y., Benítez N., 2011, MNRAS, 410, 1939
Zitrin A. et al., 2012a, ApJ, 747, L9
Zitrin A. et al., 2012b, ApJ, 749, 97

This paper has been typeset from a TEX/LATEX file prepared by the author.